

# Eulerian and modified Lagrangian approaches to multi-dimensional condensation and collection

Xiang-Yu Li<sup>1,2,3,4</sup>, A. Brandenburg<sup>2,3,5,6</sup>, N. E. L. Haugen<sup>7,8</sup>, and G. Svensson<sup>1,3,9</sup>

<sup>1</sup>Department of Meteorology, and Bolin Centre for Climate Research, Stockholm University, Stockholm, Sweden

<sup>2</sup>Nordita, KTH Royal Institute of Technology and Stockholm University, 10691 Stockholm, Sweden

<sup>3</sup>Swedish e-Science Research Centre, www.e-science.se, Stockholm, Sweden

<sup>4</sup>Laboratory for Atmospheric and Space Physics, University of Colorado, Boulder, CO 80303, USA

<sup>5</sup>JILA and Department of Astrophysical and Planetary Sciences University of Colorado, Boulder, CO 80303, USA

<sup>6</sup>Department of Astronomy, Stockholm University, SE-10691 Stockholm, Sweden

<sup>7</sup>SINTEF Energy Research, 7465 Trondheim, Norway

<sup>8</sup>Department of Energy and Process Engineering, NTNU, 7491 Trondheim, Norway

<sup>9</sup>Global & Climate Dynamics, National Center for Atmospheric Research, Boulder, CO 80305, USA

## Key Points:

- Eulerian Smoluchowski and Lagrangian superdroplet/superparticle approaches to cloud droplet growth through condensation and collection are compared using DNS techniques
- Size spectra agree well for both approaches, especially in case of turbulence
- The Lagrangian scheme with symmetric collection is found to be optimal and computationally most efficient

arXiv:1604.08169v3 [physics.flu-dyn] 26 Jan 2017

## Abstract

Turbulence is argued to play a crucial role in cloud droplet growth. The combined problem of turbulence and cloud droplet growth is numerically challenging. Here, an Eulerian scheme based on the Smoluchowski equation is compared with two Lagrangian superparticle (or superdroplet) schemes in the presence of condensation and collection. The growth processes are studied either separately or in combination using either two-dimensional turbulence, a steady flow, or just gravitational acceleration without gas flow. Good agreement between the different schemes for the time evolution of the size spectra is observed in the presence of gravity or turbulence. Higher moments of the size spectra are found to be a useful tool to characterize the growth of the largest drops through collection. Remarkably, the tails of the size spectra are reasonably well described by a gamma distribution in cases with gravity or turbulence. The Lagrangian schemes are generally found to be superior over the Eulerian one in terms of computational performance. However, it is shown that the use of interpolation schemes such as the cloud-in-cell algorithm is detrimental in connection with superparticle or superdroplet approaches. Furthermore, the use of symmetric over asymmetric collection schemes is shown to reduce the amount of scatter in the results.

## 1 Introduction

In the context of raindrop formation, it is generally accepted that turbulence plays a crucial role in bridging the size gap between efficient condensational growth of small particles (radii below  $10\ \mu\text{m}$ ) and efficient collectional growth due to gravity of larger ones (radii around  $100\ \mu\text{m}$  and above) [Shaw, 2003; Grabowski and Wang, 2013; Khain *et al.*, 2007]. Improving the understanding of this important problem in meteorology [Berry and Reinhardt, 1974; Pinsky and Khain, 1997; Falkovich *et al.*, 2002; Naumann and Seifert, 2016a] might also shed light on how to bridge the even more severe size gap in the astrophysical context of planetesimal formation [Johansen *et al.*, 2007, 2012]. To address these questions numerically, one has to combine direct numerical simulations (DNS) of turbulent gas motions with those of particles. The particles are cloud droplets in the meteorological context and dust grains in astrophysics. A possible approach to treat collection is to solve the Smoluchowski equation (also known as the stochastic collection equation in the meteorological context) [Ogura and Takahashi, 1973; Svensson and Seinfeld, 2002; Bec *et al.*, 2016], which couples the spatio-temporal evolution equations of the particle distribution function for different particle sizes. The particle motion can be treated using a fluid description for each particle size. Thus, not only does one have to solve the Smoluchowski equation at each meshpoint, but, because heavier particles have finite momenta and speeds that are different from those of the gas, one has to solve corresponding momentum equations for each mass species. In the meteorological context, it is also referred to as a binned spectral method, although in that case the momentum equations for the particle bins are normally ignored [Xue *et al.*, 2008]. An Eulerian approach is technically more straightforward than a Lagrangian one, but it becomes computationally demanding as the size range of cloud droplets is large.

The Eulerian approach also has conceptual difficulties if the collection probability depends on the mutual velocity difference. This is due to the fact that particles of the same size are described by the same momentum equation and have therefore the same velocity at a given position in space, so the velocity difference vanishes. This means that particles of the same size are not allowed to collide. This is not a problem for freely falling particles of the same size, which would have the same terminal velocity and are not expected to collide. This would however be an unrealistic restriction when particles are subject to acceleration by turbulence. More importantly, as was emphasized in the recent review of Khain *et al.* [2015], the Smoluchowski equation is a mean-field equation and cannot capture the random properties of the collections if the collision kernel is prescribed a priori. Nevertheless, most numerical cloud microphysical approaches are based on the Smoluchowski equation, which therefore raises questions regarding the accuracy of the basic equations Khain *et al.* [2015]. Thus, new

approaches based on inherently different equations are required to model the cloud microphysical processes.

An alternative approach is the Lagrangian one, where one solves for the motion of individual particles and treats collections explicitly. In atmospheric clouds, the number density of micrometer-sized cloud droplets is of the order of  $10^8 \text{ m}^{-3}$ , so in a volume of  $1 \text{ m}^3$ , one has 100 million particles, which is the typical size that can be treated on modern supercomputers. A domain of this size is also about the largest that is possible in direct numerical simulations (DNS) of atmospheric turbulence; the Reynolds number based on the length scale  $\ell = 1 \text{ m}$  and the corresponding velocity scale  $u_\ell \approx 0.2 \text{ m/s}$  is  $u_\ell \ell / \nu \approx 20,000$ , where  $\nu \approx 10^{-5} \text{ m}^2 \text{ s}^{-1}$  is the viscosity of the gas flow. Such a large Reynolds number is just within reach on current supercomputers, but larger domains would remain out of reach for a long time. Several earlier works investigated condensational growth of cloud droplets using Lagrangian tracking in DNS [Paoli and Shariff, 2009; Sardina et al., 2015; de Lozar and Muessle, 2016; Lanotte et al., 2009], but those neglected the collectional growth and only proposed to study the collectional growth in future work. An intermediate approach involves the use of Lagrangian “superparticles” [Johansen et al., 2012; Pruppacher and Klett, 2012; Shima et al., 2009; Zsom and Dullemond, 2008], which represent a “swarm” of particles of certain size and number density. Depending on the values of particle size and number density, there is a certain probability that an encounter between two superparticles leads to collectional growth of some of the particles in each swarm (or superparticle). This superparticle approach has been applied in a recent LES model to represent the cloud microphysical condensation [Andrejczuk et al., 2008] and collection [Andrejczuk et al., 2010; Riechelmann et al., 2012; Naumann and Seifert, 2015] processes.

The purpose of the present paper is to compare the Eulerian approach involving the Smoluchowski equation with the Lagrangian superparticle approach with the aim of identifying a promising DNS scheme for tackling the bottleneck problem of cloud droplets growth. This has been done in the astrophysical context [Ohtsuki et al., 1990; Drążkowska et al., 2014], where the principal problem with the Eulerian approach was emphasized in that it requires high mass bin resolution (MBR) to avoid artificial speedup of the growth rate. Here we also compare with the superdroplet approach of Shima et al. [2009]. The original work on this approach was restricted to the case of vanishing particle inertia, but this restriction is not a principal limitation of this scheme, which is in fact well applicable to the case of finite particle inertia.

## 2 Lagrangian and Eulerian approaches

In the following, we refer to the superparticle or superdroplet approaches as the *swarm model*, where each superparticle represents a swarm of physical particles. By contrast, the Eulerian approach is also referred to as the *Smoluchowski model*. Here we compare the two approaches in the meteorological context of water droplets using, however, simplifying assumptions such as constant supersaturation and ideal collection efficiency. In this paper, we generally refer to particles and superparticles, which are thus used interchangeably with droplets and superdroplets, respectively. We begin with a discussion of the gas flows that are being used in some of the models.

### 2.1 Evolution equations for the gas flow in both approaches

In all the experiments reported below, where a nonvanishing gas flow is used, we restrict ourselves to two-dimensional (2-D) flows. However, we also perform several experiments with no gas flow ( $\mathbf{u} = 0$ ). In those cases the system is spatially uniform and therefore zero-dimensional (0-D). For the swarm model, however, each swarm occupies one grid cell, so it must be treated in at least one dimension (1-D), although the results of higher-dimensional swarm models will also be discussed, and they are computational cheaper because they can

take advantage of better parallelization. By comparison, the Eulerian models are strictly 0-D when there is no flow.

### 2.1.1 Momentum equation of the gas flow

To obtain  $\mathbf{u}$  at each meshpoint, we solve the usual Navier-Stokes equation

$$\frac{\partial \mathbf{u}}{\partial t} + \mathbf{u} \cdot \nabla \mathbf{u} = \mathbf{f} - \rho^{-1} \nabla p + \mathbf{F}(\mathbf{u}), \quad (1)$$

where  $\mathbf{f}$  is a forcing term,  $p$  is the gas pressure,  $\rho$  is the gas density, which in turn obeys the continuity equation,

$$\frac{\partial \rho}{\partial t} + \nabla \cdot (\rho \mathbf{u}) = 0, \quad (2)$$

the viscous force  $\mathbf{F}(\mathbf{u})$  is given by

$$\mathbf{F}(\mathbf{u}) = \nu(\nabla^2 \mathbf{u} + \frac{1}{3} \nabla \nabla \cdot \mathbf{u} + 2\mathbf{S} \cdot \nabla \ln \rho), \quad (3)$$

where  $S_{ij} = \frac{1}{2}(u_{i,j} + u_{j,i}) - \frac{1}{3} \delta_{ij} \nabla \cdot \mathbf{u}$  is the traceless rate-of-strain tensor and commas denote partial differentiation. We assume that the gas is isothermal and has constant sound speed  $c_s$  so that the pressure  $p = c_s^2 \rho$  is proportional to the gas density  $\rho$ . Note that gravity has been neglected in equation (1), but this is not a principal restriction and can be relaxed once suitable non-periodic boundary conditions are adopted. For the relatively small domains that can be handled by DNS, gravity will nevertheless have only minor effects on the fluid flow for atmospheric conditions.

### 2.1.2 Straining flow

To obtain a non-vanishing flow, we apply volume forcing via the term  $\mathbf{f}$ . In the case of a time-independent 2-D divergence-free straining flow,

$$\mathbf{u}_{\text{str}} = u_0 (\sin kx \cos kz, 0, -\cos kx \sin kz), \quad (4)$$

we take  $\mathbf{f} = \nu k^2 \mathbf{u}_{\text{str}}$ , where  $u_0$  determines the amplitude and  $k$  the wavenumber of the flow.

### 2.1.3 Turbulence

In the case of a turbulent flow,  $\mathbf{f}$  is delta-correlated in time and consists of random waves in space [Haugen *et al.*, 2004]. The flow is characterized by a typical forcing wavenumber  $k_f$  ( $\sqrt{2}k$  for the straining flow or the average wavenumber from a narrow band of wavevectors) and the root-mean-square (rms) velocity  $u_{\text{rms}}$ . As a relevant timescale characterizing such a flow, we define

$$\tau_{\text{cor}} = (u_{\text{rms}} k_f)^{-1}, \quad (5)$$

which is an estimate of the correlation time. This definition is also used for the straining flow, which is a special case in that it is time-independent and therefore  $\tau_{\text{cor}}$  would no longer characterize the correlation time of the flow, but it would still be proportional to the turnover time. A simulation without spatial extent can be adopted to investigate the statistical convergence properties of the Eulerian model regarding its computational efficiency.

## 2.2 Condensational growth

The growth of the particle radius  $r_i$  by condensation is governed by [Lamb and Verlinde, 2011]

$$\frac{dr_i}{dt} = \frac{Gs}{r_i}, \quad (6)$$

where  $s$  is the supersaturation and  $G$  is the condensation parameter. Both  $s$  and  $G$  are in principle dependent on the flow and the environmental temperature and pressure [see Chapter 8

of *Lamb and Verlinde, 2011*], but these dependencies are here neglected, because it would complicate the comparison of different numerical schemes even further. Therefore, the condensational growth is driven by constant water vapor flux without latent heat release in the present study. We adopt the value  $G = 5 \times 10^{-11} \text{ m}^2 \text{ s}^{-1}$  [*Lanotte et al., 2009*]. The assumed constancy of  $s$  also implies that the total liquid water content is not conserved.

### 2.3 The swarm model

The swarm model is a Monte Carlo type approach that handles particle collections in a swarm of particles in a statistical manner [*Zsom and Dullemond, 2008*]. Each swarm  $i$  has a particle number density  $n_i$ , and occupies a volume  $\delta x^D$ , which equals the volume of a fluid grid cell of size  $\delta x$  in  $D$  dimensions. All particles in a given swarm have the same mass, radius, and velocity. Following the description of *Johansen et al.* [2012], the swarm is transported along with its “shepherd particle”, which is also referred to as the corresponding superparticle. The swarm is treated as a Lagrangian point-particle, where one solves for the particle position  $\mathbf{x}_i$  via

$$\frac{d\mathbf{x}_i}{dt} = \mathbf{V}_i \quad (7)$$

and the velocity via

$$\frac{d\mathbf{V}_i}{dt} = \frac{1}{\tau_i}(\mathbf{u} - \mathbf{V}_i) + \mathbf{g} \quad (8)$$

in the usual way. Here,  $\mathbf{g}$  is the gravitational acceleration,  $\tau_i$  is the particle inertial response or stopping time of a particle in swarm  $i$  and is given by

$$\tau_i = \frac{2\rho_s r_i^2}{9\rho\nu_i^{\text{eff}}}, \quad (9)$$

where  $r_i$  is the radius of particles in swarm  $i$ ,  $\rho_s$  is the particle solid material density,  $\rho$  is the density of the gas and the effective viscosity is given by *Sullivan et al.* [1994]

$$\nu_i^{\text{eff}} = \nu(1 + 0.15 \text{Re}_i^{0.687}), \quad (10)$$

where  $\nu$  is the ordinary (microphysical) fluid viscosity, and  $\text{Re}_i = 2r_i|\mathbf{u} - \mathbf{V}_i|/\nu$  is the particle Reynolds number, which provides a correction factor to the particle stopping time.

A given swarm may only interact with every other swarm within the same grid cell. The computational cost associated with such collections scales as  $N_{pg}^2$ , where  $N_{pg}$  is the number of swarms within a grid cell, but this is computationally not prohibitive as long as  $N_{pg}$  is not too large.

We now consider two swarms  $i$  and  $j$  residing within the same grid cell. Consider first collections of particles within swarm  $j$  with a particle of swarm  $i$ . The inverse mean free path of  $i$  in  $j$  is given by

$$\lambda_{ij}^{-1} = \sigma_{ij} n_j E_{ij}, \quad (11)$$

where  $\sigma_{ij}$  is the collectional cross section with

$$\sigma_{ij} = \pi(r_i + r_j)^2, \quad (12)$$

and  $E_{ij}$  is the collision efficiency, but in the following we assume  $E_{ij} = 1$  in all cases.<sup>1</sup> The particle number density in swarm  $j$  is  $n_j$  and  $r_i$  and  $r_j$  represent the radii of the particles in the two swarms. From this, one can find the typical rate of collections between a particle of swarm  $i$  and particles of swarm  $j$  as

$$\tau_{ij}^{-1} = \lambda_{ij}^{-1} |\mathbf{V}_i - \mathbf{V}_j| = \sigma_{ij} n_j |\mathbf{V}_i - \mathbf{V}_j| E_{ij}, \quad (13)$$

<sup>1</sup> In *Shima et al.* [2009], the mean free path is defined by invoking the swarm with the larger number density of physical particles; see section 2.3.2 for details.

where  $V_i$  and  $V_j$  are the velocities of swarms  $i$  and  $j$ . The probability of a collection between the swarm  $i$  and any of the particles of swarm  $j$  within the current time step  $\Delta t$  is then given by

$$p_{ij} = \tau_{ij}^{-1} \Delta t. \quad (14)$$

This effectively puts a restriction on the time step, since the probability cannot be larger than unity. For each swarm pair in a grid cell, one now picks a random number,  $\eta_{ij}$ , and compares it with  $p_{ij}$ . A collection event occurs in the case when  $\eta_{ij} < p_{ij}$ .

### 2.3.1 Collection scheme I

For the swarm model, two different collection schemes have been proposed in the astrophysical and meteorological contexts. We begin discussing the former (scheme I), which is similar to that described by *Johansen et al.* [2012] in that it maintains a constant mass of the individual swarms. In the context of mathematical probability, this approach is also known as mass flow algorithm [*Eibeck and Wagner*, 2001; *Patterson et al.*, 2011]. Scheme II is discussed in section 2.3.2.

If  $\eta_{ij} < p_{ij}$ , one assumes that *all* the particles in swarm  $i$  have collided with a particle in swarm  $j$ . In this collection scheme, all swarms are treated individually. This means that even though the particles in swarm  $i$  have collided with the particles in swarm  $j$ , swarm  $j$  is kept unchanged at this stage. Instead, swarm  $j$  is treated individually at a different stage. Hence, all collections are asymmetric, i.e.,  $p_{ij} \neq p_{ji}$ . The new mass of the particles in swarm  $i$  now becomes

$$\tilde{m}_i = m_i + m_j, \quad (15)$$

where  $m_i$  is the mass before the collection and the tilde represents the new value after collection. In order to ensure mass conservation, the *total* mass of swarm  $i$  is kept unchanged, i.e.,

$$\tilde{n}_i \tilde{m}_i = n_i m_i, \quad (16)$$

which implies that the new particle number density,  $\tilde{n}_i$ , is given by  $\tilde{n}_i = n_i m_i / \tilde{m}_i$ ; see equation (17) of *Patterson et al.* [2011] for the corresponding treatment in the mass flow algorithm. By invoking momentum conservation,

$$\tilde{V}_i \tilde{m}_i = V_i m_i + V_j m_j, \quad (17)$$

the new velocity of any particle in swarm  $i$  is given by  $\tilde{V}_i = (V_i m_i + V_j m_j) / \tilde{m}_i$ .

### 2.3.2 Collection scheme II

In the meteorological context, the following collection scheme has been proposed [*Shima et al.*, 2009]. Assume two swarms  $i$  and  $j$ , and consider (without loss of generality) the case  $n_j > n_i$ . The collection probability of particles in swarm  $i$  with swarm  $j$  is, again, given by equation (14). If the two swarms are found to collide, the new masses of the particles in the two swarms are given by

$$\begin{aligned} \tilde{m}_i &= m_i + m_j, \\ \tilde{m}_j &= m_j, \end{aligned} \quad (18)$$

but now their new particle number densities are

$$\begin{aligned} \tilde{n}_i &= n_i, \\ \tilde{n}_j &= n_j - n_i. \end{aligned} \quad (19)$$

In other words, the number of particles in the smaller swarm remains unchanged (and their masses are increased), while that in the larger one is reduced by the amount of particles that have collided with all the particles of the smaller swarm (and their masses remain unchanged).

This implies that in equation (11), the mean free path is defined with respect to the swarm with the larger number density of physical particles, as explained in *Shima et al.* [2009]. Finally, the new momenta of the particles in the two swarms are given by

$$\begin{aligned}\tilde{\mathbf{V}}_i \tilde{m}_i &= \mathbf{V}_i m_i + \mathbf{V}_j m_j, \\ \tilde{\mathbf{V}}_j \tilde{m}_j &= \mathbf{V}_j m_j.\end{aligned}\quad (20)$$

In contrast to scheme I, these collections are symmetric, i.e.  $p_{ij} = p_{ji}$ . Consequently, both swarms are changed during a collection. However, the asymmetric collection property of scheme I of [*Johansen et al.*, 2012] may not have been previously recognized, nor has its accuracy been compared with other models, which we will further discuss below.

### 2.3.3 Initial particle distribution

We recall that particles within a swarm may interact with particles of another swarm only if both swarms occupy the same grid cell. The effective volume of each swarm is therefore equal to  $\delta x^D$ , where  $D$  is the spatial dimension introduced in section 2.3. The total number of particles in our computational domain is therefore  $\delta x^D$  times the sum of  $n_i$  over all  $N_p$  swarms. This must also be equal to  $nL^D$ , where  $n$  is the total number density represented by the simulation and  $L$  is the size of the computational domain. Thus, we have

$$nL^D = \delta x^D \sum_{i=1}^{N_p} n_i. \quad (21)$$

Initially ( $t = 0$ ), the particle number densities of all swarms are the same and since  $(L/\delta x)^D = N_{\text{grid}}$  is the total number of grid points, we have  $nN_{\text{grid}} = n_i N_p$ . Thus, the initial number density of particles within one swarm must be

$$n_i = nN_{\text{grid}}/N_p \quad (\text{at } t = 0). \quad (22)$$

In the following, we choose the initial particle size distribution of total physical particles in the domain to be log-normal, i.e.,

$$f(r_i, 0) = \left( n_0 / (\sqrt{2\pi}\sigma_p r) \right) \exp \left\{ -[\ln(r_i/r_{\text{ini}})]^2 / 2\sigma_p^2 \right\}, \quad (23)$$

where  $r_{\text{ini}}$  and  $\sigma_p$  are the center and width of the size distribution, respectively;  $n_0 = n(t = 0)$  is the initial total number density of physical particles. These particles are distributed uniformly over all swarms within the computational domain. This means that particles in each swarm are of the same size, but different from swarm to swarm.

## 2.4 Eulerian approach

To model the combined growth of particles through condensation and collection in a multi-dimensional flow in the Eulerian description, we describe the evolution of particles of different radii  $r$  (or, equivalently, of different logarithmic particle mass  $\ln m$ ) at different positions  $\mathbf{x}$  and time  $t$ . We employ the particle distribution function  $f(\mathbf{x}, r, t)$ , or, alternatively in terms of logarithmic particle mass  $\ln m$ ,  $\tilde{f}(\mathbf{x}, \ln m, t)$ , such that the total number density of particles is given by

$$n(\mathbf{x}, t) = \int_0^\infty f(\mathbf{x}, r, t) dr, \quad (24)$$

or, correspondingly for  $\tilde{f}$ , we have  $n(\mathbf{x}, t) = \int_{-\infty}^\infty \tilde{f}(\mathbf{x}, \ln m, t) d \ln m$ . Since  $m = 4\pi r^3 \rho_s / 3$ , we have  $\tilde{f} = f dr / d \ln m = fr/3$ . Note that  $n(\mathbf{x}, t)$  obeys the usual continuity equation,

$$\frac{\partial n}{\partial t} + \nabla \cdot (n\bar{\mathbf{v}}) = D_p \nabla^2 n, \quad (25)$$

where  $\bar{\mathbf{v}}$  is the mean particle velocity (i.e., an average over all particle sizes) and  $D_p$  is a Brownian diffusion term, which is enhanced for numerical stability and will be chosen depending

on the mesh resolution. The evolution of the particle distribution function is governed by a similar equation, but with additional coupling terms due to condensation and collection, i.e.

$$\frac{\partial f}{\partial t} + \nabla \cdot (f\mathbf{v}) + \nabla_r(fC) = \mathcal{T}_{\text{coll}} + D_p \nabla^2 f, \quad (26)$$

where  $\nabla_r = \partial/\partial r$  is the derivative with respect to  $r$ ,  $C \equiv dr/dt = Gs/r$ , as given in equation (6), and  $\mathcal{T}_{\text{coll}}$  describes the change of the number density of particles for smaller and larger radii, as will be defined below. Furthermore,  $\mathbf{v}(\mathbf{x}, r, t)$  is the particle velocity within the resolved grid cell, which is discussed below. It also determines the mean flow  $\bar{\mathbf{v}} = \int f\mathbf{v} dr/n$  in equation (25).

The modeling of condensation and collection implies coupling of the evolution equations of  $f(\mathbf{x}, r, t)$  for different values of  $r$ . The advantage of using  $\tilde{f}(\mathbf{x}, \ln m, t)$  is that it allows us to cover a large range in  $m$ , because we will use then an exponentially stretched grid in  $m$  such that  $\ln m$  is uniformly spaced [Pruppacher and Klett, 2012; Suttner and Yorke, 2001; Johansen, 2004]. The total number density within a finite mass interval  $\delta \ln m$  is then given by  $\tilde{f}(\mathbf{x}, \ln m, t) \delta \ln m$ . Thus, the total number density of particles of all sizes at position  $\mathbf{x}$  and time  $t$  is given by

$$n(\mathbf{x}, t) = \sum_{k=1}^{k_{\text{max}}} \tilde{f}_k \delta \ln m = \sum_{k=1}^{k_{\text{max}}} \hat{f}_k, \quad (27)$$

where  $\hat{f}_k = \tilde{f}(\ln m_k) \delta \ln m$  is the variable used in the simulations and  $k_{\text{max}}$  is the number of logarithmic mass bins.

Let us first consider the process of condensation, which is described in equation (26) by the term  $\nabla_r(fC)$ , where  $fC$  is the flux of particle from one size bin to the next. Evidently, the total number density is only conserved if the particle flux  $fC$  vanishes for  $r = r_{\text{min}}$  and  $r = r_{\text{max}}$ , which is the case if the range of  $r$  is sufficiently large. In particular,  $(fC)_{\text{min}} \rightarrow 0$ , because  $n \rightarrow 0$  for  $m \rightarrow 0$ . In practice, however, we consider finite lower cutoff values of  $m$  and therefore expect some degree of mass loss at the smallest mass bins. The same is also true for the largest mass bin once the size distribution has grown to sufficiently large values. In all cases with pure condensation, it is convenient to display solutions in non-dimensional form by measuring time in units of

$$\tau_{\text{cond}} = r_{\text{ini}}^2 / 2Gs \quad (28)$$

and  $r$  in units of  $r_{\text{ini}}$ . We refer to Appendix A for more details on the condensation equation for the Eulerian approach.

Next, we consider collection, which leads to a decrease of  $n$ , but does not change the mean mass density of liquid water. The evolution of  $\tilde{f}(\mathbf{x}, \ln m, t)$  due to collection is governed by the Smoluchowski equation

$$\begin{aligned} \mathcal{T}_{\text{coll}} = & \frac{1}{2} \int_0^m K(m - m', m') f(m - m') f(m') dm' \\ & - \int_0^\infty K(m, m') f(m) f(m') dm'. \end{aligned} \quad (29)$$

Here,  $K$  is a kernel, which is proportional to the collision efficiency  $E(m, m')$  and a geometric contribution. As mentioned above, we assume  $E = 1$  and so  $K$  is given by

$$K(m, m') = \pi(r + r')^2 |\mathbf{v} - \mathbf{v}'|, \quad (30)$$

where  $r$  and  $r'$  are the radii of the corresponding mass variables,  $m$  and  $m'$ , while  $\mathbf{v}$  and  $\mathbf{v}'$  are their respective velocities, whose governing equation is given below.

In the following, we define the mass and radius bins such that

$$m_k = m_1 \delta^{k-1}, \quad r_k = r_1 \delta^{(k-1)/3}. \quad (31)$$

Unfortunately,  $\delta = 2$  is in many cases far too coarse, so we take

$$\delta = 2^{1/\beta}, \quad (32)$$

where  $\beta$  is a parameter that we chose to be a power of two. For a fixed mass bin range, the number of mass bins  $k_{\max}$  increases with increasing  $\beta$ . In terms of  $\hat{f}_k$ , equation (29) reads

$$\mathcal{T}_k^{\text{coll}} = \frac{1}{2} \sum_{i+j \in k} K_{ij} \frac{m_i + m_j}{m_k} \hat{f}_i \hat{f}_j - \hat{f}_k \sum_{i=1}^{k_{\max}} K_{ik} \hat{f}_i, \quad (33)$$

where we have adopted the nomenclature of *Johansen* [2004], where  $i + j \in k$  denotes all values of  $i$  and  $j$  for which

$$m_{k-1/2} \leq m_i + m_j < m_{k+1/2} \quad (34)$$

is fulfilled. The term  $(m_i + m_j)/m_k$  in equation (33) comes from the fact that collections between cloud droplets from two mass bins may not necessarily result in a cloud droplet mass being exactly in the middle of the nearest mass bin. *Johansen* [2004] therefore included this factor so that mass is strictly conserved. The discrete kernel is then  $K_{ij} = \pi(r_i + r_j)^2 |\mathbf{v}_i - \mathbf{v}_j|$ .

The corresponding momentum equations for the velocities  $\mathbf{v}_k(\mathbf{x}, t) = \mathbf{v}(\mathbf{x}, \ln m_k, t)$  for each logarithmic mass value  $\ln m_k$  is

$$\frac{\partial \mathbf{v}_k}{\partial t} + \mathbf{v}_k \cdot \nabla \mathbf{v}_k = \mathbf{g} - \frac{1}{\tau_k} (\mathbf{v}_k - \mathbf{u}) + \mathbf{F}_k(\mathbf{v}_k) + \mathcal{M}_k, \quad 1 \leq k \leq k_{\max}. \quad (35)$$

Here,  $\mathbf{u}$  is the gas velocity,  $\tau_k$  (for  $k = i$ ) is defined by equation (9), and

$$\mathbf{F}_k(\mathbf{v}_k) = \nu_p \nabla^2 \mathbf{v}_k \quad (36)$$

is a viscous force among particles, which should be very small for dilute particle suspensions, but is nevertheless retained in equation (35) for the sake of numerical stability of the code. It is not to be confused with the drag force,  $-\tau_k^{-1}(\mathbf{v}_k - \mathbf{u})$  between particles and gas. In principle, the expression for  $\mathbf{F}_k(\mathbf{v}_k)$  should be based on the divergence of the traceless rate-of-strain tensor of  $\mathbf{v}_k$ , similarly to the corresponding expression for the viscous force of the gas discussed in equation (3). However, since the term  $\mathbf{F}_k(\mathbf{v}_k)$  is unphysical anyway, we just use the simpler expression proportional to  $\nabla^2 \mathbf{v}_k$  instead.

The linear momentum of all particles is given by  $\sum \langle \hat{f}_k m_k \mathbf{v}_k \rangle$ , where angle brackets denote volume averages. In order that this quantity is conserved by each collection, the target has to receive a corresponding kick, which leads to the last term in equation (35), but it leaves the velocities of the collection partners unchanged. It is therefore only related to the first term on the right-hand side of equation (33) and not the second, so it is given by (see Appendix B)

$$\mathcal{M}_k = \frac{1}{2 \hat{f}_k m_k} \sum_{i+j \in k} K_{ij} \hat{f}_i \hat{f}_j [m_i \mathbf{v}_i + m_j \mathbf{v}_j - (m_i + m_j) \mathbf{v}_k]. \quad (37)$$

To our knowledge, this momentum-conserving term has not been included in any of the very few earlier works that include a momentum equation for each particle species [cf. *Suttner and Yorke*, 2001; *Elperin et al.*, 2015]. The reason why this has apparently not previously been discussed in the literature is that in meteorological applications one usually works with the averaged kernel and neglects the evolution of the velocities for the different mass bins [*Grabowski and Wang*, 2013]. This correction term is evidently zero when the momentum of the two collection constituents ( $= m_i \mathbf{v}_i + m_j \mathbf{v}_j$ ) is equal to that of the resulting constituent [ $= (m_i + m_j) \mathbf{v}_k$ ]. Nevertheless, as is shown in Appendix B, the momentum conserving correction changes the time evolution of the droplet spectrum in an unexpected way when the MBR is high, but the results are similar for  $\beta = 2$ . Furthermore, for turbulent flows, as is discussed below, these correction terms become insignificant.

As mentioned above, a shortcoming of the Eulerian approach is that no collection is possible from equally sized particles. To assess the consequences of this unphysical limitation, we study the sensitivity of the results to replacing  $K_{ij}$  either (i) by  $(K_{i+1} + K_{i+1})/2$  or (ii) by  $\epsilon_{\text{self}} \pi (2r_i)^2 |\mathbf{v}_i + \mathbf{v}_j|/2$ , where  $\epsilon_{\text{self}}$  is an empirical parameter.

## 2.5 Boundary conditions and diagnostics

In the present work, we use periodic boundary conditions for all variables in all directions. Therefore, no particles and no gas are lost through the boundaries of the domain. This approximation is reasonable as long as we are interested in modeling a small domain well within a cloud where also heavier particles can be assumed to enter from above. The use of periodic boundary conditions requires us to neglect gravity in equation (1), which could be relaxed if non-periodic boundary conditions were adopted.

To characterize the size distribution, especially for the larger particles, we consider the evolution of different normalized moments of the size spectra,

$$a_\zeta = \left( \frac{\sum_{k=1}^{k_{\max}} \langle \hat{f}_k r_k^\zeta \rangle}{\sum_{k=1}^{k_{\max}} \langle \hat{f}_k \rangle} \right)^{1/\zeta}, \quad (38)$$

where  $\zeta$  is a positive integer. The mean radius  $\bar{r}$  is given by  $a_1$ . Higher moments represent the tail of the distribution at large radii. In view of raindrop formation, we will be particularly interested in the largest droplets in the distribution. However, very large moments become numerically difficult to compute accurately, but  $a_{12}$ , for example, was still not sufficiently representative of the largest droplets. Therefore we arrived at  $a_{24}$  as a reasonable compromise to characterize the largest droplets in the distribution. Alternatively, the size distribution can be characterized by a gamma distribution, which requires the determination of only three moments in an approach known as the three-moment bulk scheme [Seifert and Beheng, 2001]. This will be discussed in more detail in section 3.3.

In the case of collection, the condensation timescale  $\tau_{\text{cond}}$ , defined in equation (28), is no longer relevant, but it is instead a collection timescale that can be defined in the Eulerian model as

$$\tau_{\text{coll}}^{-1} = \frac{\sum_{k=1}^{k_{\max}} \langle \mathcal{T}_k^{\text{coll}} \rangle}{\sum_{k=1}^{k_{\max}} \langle \hat{f}_k \rangle}, \quad (39)$$

which is, in this definition, a time-dependent quantity. In the Lagrangian model, this quantity can be defined by the collection frequency. Unlike the case of pure condensation, where  $\tau_{\text{cond}}$  is the appropriate time unit,  $\tau_{\text{coll}}$  can only be used a posteriori as a diagnostic quantity. However, given that the speed of pure collection is proportional to the mean particle density  $n$ , it is often convenient to perform simulations at increased values of  $n$  and then rescale time to a fixed reference density  $n_{\text{ref}}$  and use

$$\tilde{t} = t n_0 / n_{\text{ref}}. \quad (40)$$

In the following we use  $n_{\text{ref}} = 10^8 \text{ m}^{-3}$ , which is the typical value of  $n$  in atmospheric clouds. Analogously we also define  $\tilde{\tau}_{\text{coll}} = \tau_{\text{coll}} n_0 / n_{\text{ref}}$ . Finally, the number of particles in the total simulation domain is  $N(t) = \int n(\mathbf{x}, t) d^D x$ .

## 2.6 Computational implementation

We use the PENCIL CODE<sup>2</sup>, which is a public domain code where the relevant equations have been implemented [Johansen, 2004; Johansen et al., 2004; Babkovskaia et al., 2015]. We refer to Appendix A for a description of an important modification applied to the implementation of equation (6). The implementation of equation (33) has been discussed in detail by Johansen [2004], and follows an approach described earlier by Suttner and Yorke [2001]. However, momentum conservation during collections was previously ignored in the Eulerian model. The current revision number is 73563 when checking out the code via the svn bridge on the public github repository.

<sup>2</sup> <https://github.com/pencil-code/>

**Table 1.** Summary of the simulations.

Run	Scheme	Dim	$L$ (m)	$N_p$	$N_{\text{grid}}$	IM	Processes	$\beta$	$n_0$ (m <sup>-3</sup> )	Flow	$D_p$ (m <sup>2</sup> /s)	$v_p$ (m <sup>2</sup> /s)
1A	SwI	3-D	0.5	$10^4$	$16^3$	CIC	Con	–	$10^{10}$	–		
2B	Eu	0-D	0.5	–	–	–	Con	128	$10^{11}$	–		
3C	Eu	0-D	0.5	–	–	–	Col	128	$10^{11}$	grav		
4B	SwI	3-D	0.5	$32N_{\text{grid}}$	$32^3$	CIC	Col	–	$10^{10}$	grav		
6A	SwII	3-D	0.5	$32N_{\text{grid}}$	$32^3$	CIC	Col	–	$10^{10}$	grav		
7A	SwII	2-D	$2\pi$	$3 \times 10^5$	$64^2$	CIC	Col	–	$10^{10}$	strain		
7B	SwII	2-D	$2\pi$	$3 \times 10^5$	$128^2$	CIC	Col	–	$10^{10}$	strain		
7C	SwII	2-D	$2\pi$	$3 \times 10^5$	$256^2$	CIC	Col	–	$10^{10}$	strain		
7D	Eu	2-D	$2\pi$	–	$128^2$	–	Col	2	$10^{10}$	strain	0.05	0.01
7E	SwII	2-D	$2\pi$	$3 \times 10^5$	$80^2$	NGP	Col	–	$10^{10}$	strain		
7F	SwII	2-D	$2\pi$	$3 \times 10^5$	$160^2$	NGP	Col	–	$10^{10}$	strain		
9A	SwII	2-D	$2\pi$	$5 \times 10^4$	$128^2$	CIC	Both	–	$10^8$	strain		
9B	SwII	2-D	$2\pi$	$5 \times 10^4$	$128^2$	NGP	Both	–	$10^8$	strain		
9C	Eu	2-D	$2\pi$	–	$128^2$	–	Both	2	$10^8$	strain	0.02	0.10
9D	Eu	2-D	$2\pi$	–	$128^2$	–	Both	2	$10^8$	strain	0.01	0.05
9E	Eu	2-D	$2\pi$	–	$256^2$	–	Both	2	$10^8$	strain	0.005	0.05
10A	Eu	2-D	0.5	–	$512^2$	–	Col	2	$10^{10}$	turb	0.001	0.001
10B	SwII	2-D	0.5	$1.2 \times 10^6$	$512^2$	NGP	Col	–	$10^{10}$	turb		

“IM” denotes the interpolation method, “Col” refers to collection, “Con” refers to condensation, “Eu” refers to Eulerian model, “SwI” refers to collection scheme I of swarm model, “SwII” refers to collection scheme II of swarm model, “Both” refers to condensation and collection, “grav” refers to gravity ( $\mathbf{u}=0$ ), “strain” refers to straining flow, “turb” refers to turbulence, and “Dim” refers to the dimension.

When traditional point particle Lagrangian particle tracking is employed, it is usually beneficial to employ higher order interpolation between the neighboring grid cells to find the value of a given fluid variable at the exact position of the particle. By default, the cloud-in-cell (CIC) algorithm is used, which involves first order interpolation for the particle properties on the mesh. In the swarm approach, however, the particles in each swarm fills the volume of a grid cell in which the shepherd particle is. The distribution of the swarm throughout the grid cell is homogeneous and isotropic, and as such the swarm has no particular position within the grid cell. It is true that there is a particular position associated with the swarm, namely the position of the shepherd particle, but this position has no purpose other than to determine in which grid cell the swarm resides. Below we shall show that it is *not* better to use any kind of interpolation in determining the value of the fluid variables at the position of the swarm, but rather to use the values of the grid cell in which the swarm resides. This method is technically referred to as nearest grid point mapping (NGP). Details concerning each experiment are summarized in Table 1.

### 3 Results

#### 3.1 Condensation experiments

We compare the Eulerian and Lagrangian models for the pure condensation process without motion, i.e., zero gas velocity. In the case of homogeneous condensation, we can compare the numerical solution with the analytic solution of *Seinfeld and Pandis* [2006]; see their Fig. 13.25. To this end, we make use of the fact that solutions of the condensation equation (6) obey

$$f(r, t) = (r/\tilde{r}) f(\tilde{r}, 0), \quad (41)$$

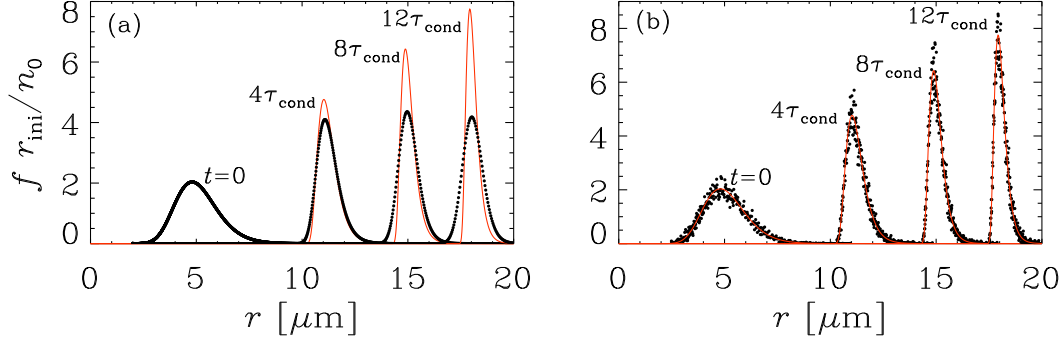


**Figure 1.** Comparison of the numerically obtained size spectra with the analytic solution for condensation with a lognormal initial condition given by  $r_{\text{ini}} = 5 \mu\text{m}$ , and  $\sigma_p = 0.2$ . Simulations of pure condensation (no turbulence nor gravity) with the Eulerian model (a) using  $\beta=128$  and  $k_{\text{max}}=1281$  mass bins in the range  $2\text{--}20 \mu\text{m}$  and the Lagrangian swarm model (b) with  $N_p = 10000$  and  $N_{\text{grid}} = 16^3$ . The solid lines correspond to the analytic solution given by equation (42) while the black dots represent the numerical results. See run 1A and 2B of Table 1 for simulation details.

where  $\tilde{r}$  is a shifted coordinate with  $\tilde{r}^2 = r^2 - 2Gst$ . With the log-normal initial distribution given by equation (23), this yields

$$f(r, t) = \frac{n_0}{\sqrt{2\pi}\sigma_p} \frac{r}{\tilde{r}^2} \exp\left[-\frac{(\ln \tilde{r} - \ln r_{\text{ini}})^2}{2\sigma_p^2}\right], \quad (42)$$

where  $r_{\text{ini}}$  denotes the position of the peak of the distribution and  $\sigma_p = \ln \sigma_{\text{SP}}$  denotes its width, where  $\sigma_{\text{SP}}$  is the symbol introduced by *Seinfeld and Pandis* [2006]. What is remarkable here is the fact that  $f(r, t)$  vanishes for  $r < r_* \equiv \sqrt{2Gst}$ . This is because in this model, no new particles are created and even particles of zero initial radius will have grown to a radius  $r_*$  after time  $t$ . Furthermore, the small particles with  $r = r_*$  grow faster than any of the larger ones, which leads to a sharp rise in the distribution function at  $r = r_*$ . Thus,  $\partial f / \partial r$  has a discontinuity at  $r = r_*$ . This poses a challenge for the Eulerian scheme in which the derivative  $\partial / \partial r$  is discretized; see equation (26). In Figure 1, we compare solutions obtained using both Eulerian and Lagrangian approaches. It is evident that the  $r$ -dependence obtained from the Eulerian solution is too smooth compared with the analytic one, even though we have used 1281 mass bins with  $\beta=128$  to represent  $r$  on our logarithmically spaced mesh over the range  $2 \mu\text{m} \leq r \leq 20 \mu\text{m}$ , which corresponds to  $\delta \approx 1.0054$ ; see equation (32). Better accuracy could be obtained by using a uniformly spaced grid in  $r$ , but this would not be useful later when the purpose is to consider collection spanning a range of several orders of magnitude in radius. By comparison, the Lagrangian solution shown in the right-hand panel of Figure 1 (here with  $n_0 = 10^{10} \text{m}^{-3}$ ) has no difficulty in reproducing the discontinuity in  $\partial f / \partial r$  at  $r = r_*$ . Moreover, the Lagrangian solution agrees perfectly with the analytical solution.

In practice, for the Eulerian approach we would use logarithmic spacing on a mesh with  $\delta = 2$  or  $2^{1/2} \approx 1.414$ . However, in such cases, the distribution develops a broad tail. This is demonstrated in detail in Appendix C. On the other hand, as we show further below, for turbulent and other velocity fields, the results depend much less on MBR so that computations with  $\beta = 2$  can be sufficiently accurate.

### 3.2 Purely gravitational collection experiments

We now consider uniform collection with no spatial variation of the velocity and density fields for both the gas and the particles. For the purely geometrical kernel, no analytic

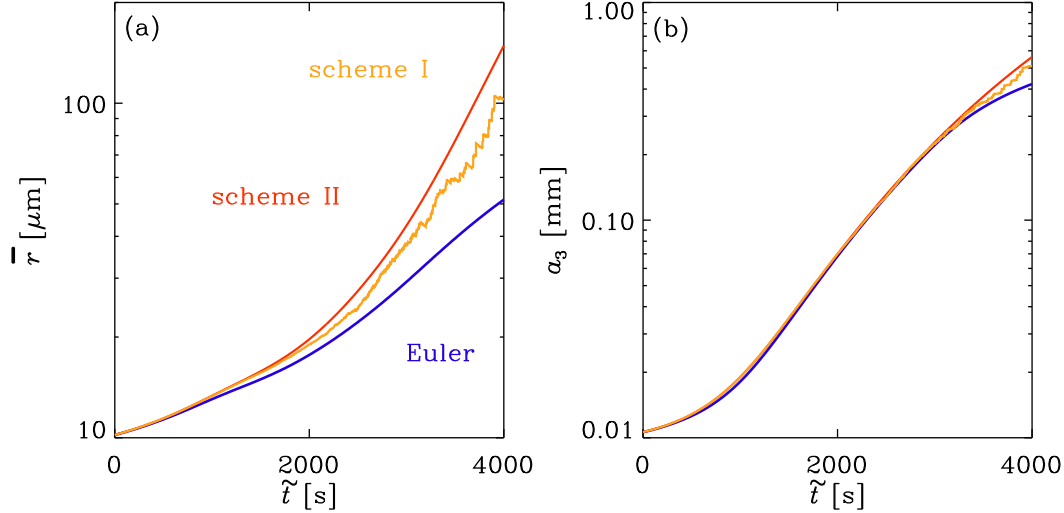


**Figure 2.** 3-D simulations with the swarm model and  $32^3$  grid points using schemes II (red) and I (orange), compared with the Eulerian model with  $\beta = 128$  (solid blue line) for (a)  $\bar{r}$  and (b)  $a_3$ . The collection is driven by gravity. See Runs 3C, 4B, and 6A of Table 1 for simulation details.

solution exists. However, we can compare the convergence properties of our two quite different numerical approaches and thereby get some sense of their validity in cases when the two agree. We consider pure collection experiments, starting again with a log-normal distribution. The results are presented in terms of normalized time; see equation (40).

### 3.2.1 Comparison between swarm collection schemes I and II

In Figure 2, we compare schemes I and II of the swarm model together with the Eulerian model. The simulations have been performed with  $N_{\text{grid}} = 32^3$  grid points and  $N_p = 32N_{\text{grid}}$  swarms (the statistics is converged for  $N_p/N_{\text{grid}} \geq 4$ , as discussed in Appendix D). The left-hand panel of Figure 2 shows that for  $\bar{r}$  the results of the swarm simulations with scheme I agree with those of scheme II at early times, but depart at late times. However, for  $a_3$ , the agreement is excellent, as shown in the right-hand panel of Figure 2. The evolution of  $\bar{r}$  with scheme I shows considerable scatter at late times. We recall that the main difference between schemes I and II is the geometry of collections. The collections simulated with scheme I are asymmetric, while those with scheme II are symmetric. Thus, in scheme II both swarms change either their total mass or their total particle number, while in scheme I the total mass of a swarm is kept constant by adjusting the particle number correspondingly. This property of scheme I may be responsible for creating stronger fluctuations in the mean radius. Therefore, to keep the amount of scatter comparable, scheme II is effectively less demanding. In the following, we will mainly adopt scheme II to save computational time.

### 3.2.2 Comparison between collection scheme II and the Eulerian model

As we have seen above, the swarm simulations follow the Eulerian results rather well for  $a_3$  (see the right-hand panel of Figure 2), but are somewhat different for  $\bar{r}$ . At early times, on the other hand, the evolution of  $\bar{r}$  obtained with the swarm model with collection scheme I follows more closely that of the Eulerian model. However, at later times, the evolution of  $\bar{r}$  obtained with the swarm model departs from the one simulated with the Eulerian model. This is surprising and might hint at a false convergence behavior, especially of the swarm model

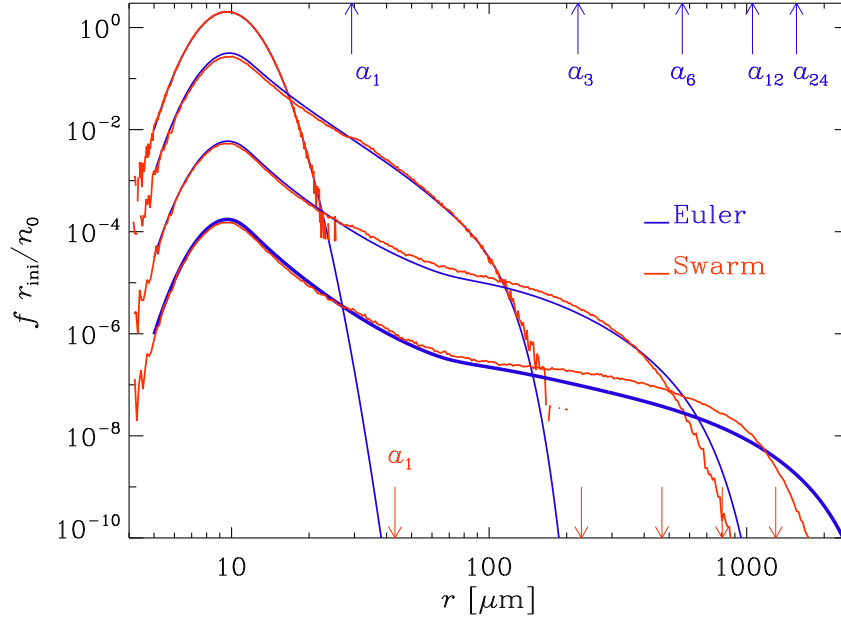


**Figure 3.** Same simulations as in Figure 2, but here we only compare scheme II with the Eulerian model. Size spectra are given for  $\tilde{t}=0$  s, 1000 s, 2000 s and 3000 s. The arrows show the values of  $a_1$ ,  $a_3$ ,  $a_6$ ,  $a_{12}$ , and  $a_{24}$  for  $\tilde{t}=3000$  s.

which has very few particles at small radii. This interpretation is supported by the fact that at larger radii the agreement is better, which also is the physically more relevant case.

We show in Appendix E that, in the case of purely gravity-driven collections,  $\bar{r}$  converges only for very large MBR. Thus, the MBR dependency of the numerical solution using the Smoluchowski scheme appears to be a serious obstacle in studying particle growth not only by condensation, but also by collection. This is a strong argument in favor of the Lagrangian scheme. The evolution of  $a_3$ , on the other hand, agrees rather well between the swarm and Eulerian models.

We emphasize that  $\bar{r}$  is sensitive to subtle changes in the size distribution, but it is at the same time not really relevant to characterizing the collectional growth toward large particles. As is shown in the following sections, the mean particle radius often increases by not much more than a factor of three (see also the left-hand panel of Figure 2), while the size distribution can become rather broad and its tail can reach the size of raindrops within a relatively short time. In addition to the mean radius, we now also consider size spectra to address the collectional growth to larger particles.

The evolution of size spectra simulated with the Eulerian scheme with 3457 mass bins ( $\beta = 128$ ) is shown as blue lines in Figure 3, while the corresponding size spectra obtained with the swarm model (collection scheme II) with 32 particles per grid point are shown as red curves. The agreement between the Eulerian and Lagrangian schemes is good at early times ( $\tilde{t} \leq 2000$  s), but at late times ( $\tilde{t} = 3000$  s) the size spectra from the Eulerian approach is broader for the largest sizes ( $r_{\max} = 1000 \mu\text{m}$ ). *Shima et al.* [2009] found that the results of the super-droplet method (collection scheme II) agree fairly well with the numerical solution of a binned spectral method. It is interesting to note that the size spectra simulated with the swarm model (scheme II) converge to those obtained with the Eulerian model with increasing  $N_p/N_{\text{grid}}$ . This can simply be explained by the fact that more swarms contribute as potential

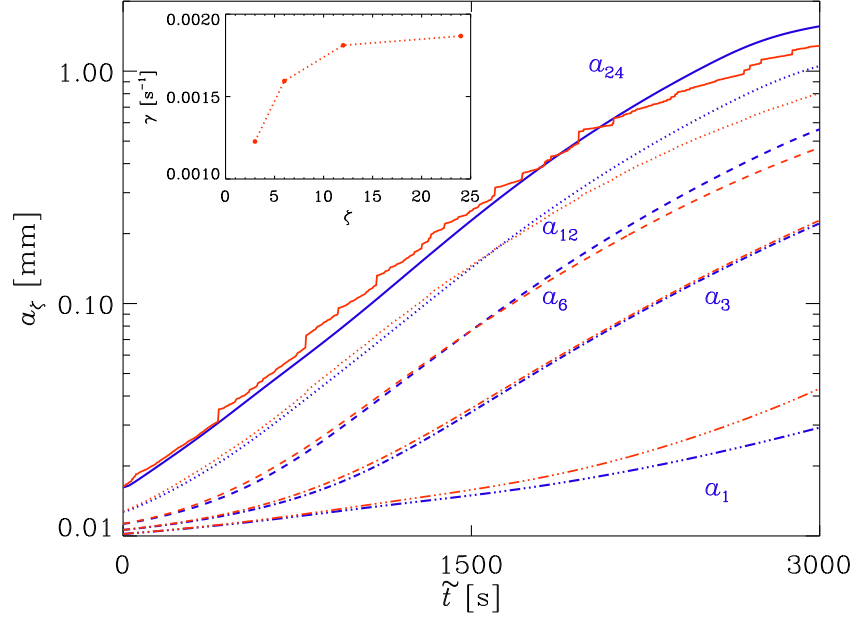


**Figure 4.** Same simulations as in Figure 2, but here we only compare the scheme II and the Eulerian model. Time evolution of  $a_1$  (three-dotted dashed line),  $a_3$  (dash-dotted lines),  $a_6$  (dash lines),  $a_{12}$  (dotted lines), and  $a_{24}$  (solid lines) of the size spectra are given. The inset shows the growth rates, for several moments (fitted between  $r=50 \mu\text{m}$  and  $r=200 \mu\text{m}$ ).

collectional partners and thus ensure more reliable statistics, which was also shown in the work of *Shima et al.* [2009].

### 3.3 Characterizing the size spectra

#### 3.3.1 Estimating the extent of the size distribution

The size spectra obtained in our simulations are rather broad and cover nearly three orders of magnitude in radius (and six in mass). Even at  $\tilde{t} = 3000 \text{ s}$ , the mean radius,  $\bar{r} = a_1$ , has barely reached  $30 \mu\text{m}$  (see Figure 2) and does not give any indication about the width of the distribution. The values of the higher moments  $a_3$  and  $a_6$  lie still only in the middle of the size range; see Figure 3, where we have marked the values of  $a_1$ ,  $a_3$ ,  $a_6$ ,  $a_{12}$ , and  $a_{24}$  by arrows for  $\tilde{t} = 3000 \text{ s}$ . We see that the value  $a_{24} \approx 1.5 \text{ mm}$  characterizes rather well the maximum radius of the distribution. The actual maximum is at  $\approx 2.4 \text{ mm}$ , but this value is rather noisy, because it represents only a single data point in our simulated volume. We have seen that our smallest and largest moments,  $a_1$  and  $a_{24}$ , conveniently bracket the extent of the size distribution. However, for the type of size spectra presented here, the higher moments do not contain any new or independent information, because all moments grow exponentially at nearly the same rate; see Figure 4. This is quantified by the instantaneous growth rates,  $\gamma(\zeta) = d\ln(a_\zeta)/dt$ , which are found to be around  $0.0018 \text{ s}^{-1}$  for large moments  $\zeta$ . Thus, at least in the range  $1000 \text{ s} \leq \tilde{t} \leq 3000 \text{ s}$ , the value of  $a_{24}$  is always approximately ten times larger than  $a_3$ . However, this ratio can be different in different cases. Knowing therefore the values of  $a_1$  and  $a_{24}$  gives a fairly reliable indication about the full extent of the size spectra.

Given that the different moments are not independent, it should not be too surprising that useful information can already be extracted from the first three moments, which is at the

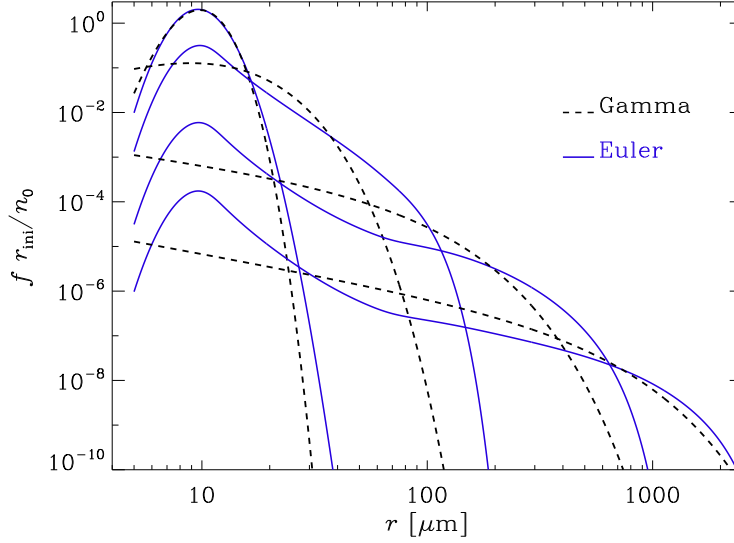


**Figure 5.** Same Eulerian simulation as in Figure 2. The black lines show the gamma distribution estimated from the Eulerian simulation.

heart of the so-called three-moment bulk scheme [Naumann and Seifert, 2016b]. This will be discussed next.

### 3.3.2 Description in terms of the gamma distribution

In the meteorological context, size spectra are often fitted to a gamma distribution [Berry and Reinhardt, 1974; Geoffroy et al., 2010],

$$f(r) = nr^\mu e^{-\lambda r} \lambda^{\mu+1} / \Gamma(\mu + 1). \quad (43)$$

Here, the factor  $\lambda^{\mu+1} / \Gamma(\mu + 1)$ , with  $\Gamma$  being the gamma function, is included so  $f(r)$  is normalized such that  $\int_0^\infty f(r) dr = n$ . In addition to  $n$ , it has  $\mu$  and  $\lambda$  as independent parameters, which are all functions of time. These are the basic parameters of the three-moment bulk scheme [Naumann and Seifert, 2016b]. An advantage of using the gamma distribution lies in the fact that all moments can be calculated analytically. Thus, one may ask for which values of  $n$ ,  $\mu$  and  $\lambda$  do the moments of the gamma distribution agree with those obtained here. For given values of  $a_1$  and  $a_2$ , we have

$$\mu = -\frac{(a_2/a_1)^2 - 2}{(a_2/a_1)^2 - 1} = -\frac{a_2^2 - 2a_1^2}{a_2^2 - a_1^2} \quad \text{and} \quad \lambda = \frac{\mu + 1}{a_1} = \frac{a_1}{a_2^2 - a_1^2}. \quad (44)$$

As stated above, the value of  $n$  is given by the zeroth moment. In Table 2 we give the values of  $n$  together with selected normalized moments  $a_\zeta$  as well as the resulting parameters  $\mu$  and  $\lambda$ . We also give  $\lambda^{-1}$ , which has units of length and can be compared with the normalized moments  $a_\zeta$ .

Note that the value of  $\mu$  decreases with time and approaches  $-1$ . At the same time,  $\lambda^{-1}$  increases and reaches  $360 \mu\text{m}$  at the last time. Although  $\lambda^{-1}$  has units of length and tends to give an indication about the cutoff of the distribution, its value is still five times smaller than that of  $a_{24}$  and thus far away from the maximum droplet radius. This reinforces us in regarding  $a_{24}$  as a useful measure of the largest droplets.

It turns out that the resulting profiles of the gamma distribution capture the broad tail of the distribution remarkably. This is shown in Figure 5, where we compare with the actual

size spectra. It is obvious that the actual size distribution shows additional bumps, notably at  $\approx 10\ \mu\text{m}$ . This is completely missed when the parameters of the gamma distribution are computed from the full data set. Note also that we have employed a double-logarithmic representation in Figure 5. To model the bump at  $10\ \mu\text{m}$ , one could again use the gamma distribution, but now with moments that are based on  $f(r)$  in a restricted size range,  $r \leq 30\ \mu\text{m}$ , for example. This type of approach has been used by *Seifert and Beheng* [2001], where they describe the size spectra of cloud droplets and raindrops with different distributions.

*Naumann and Seifert* [2016b] also found reasonable agreement between numerical obtained size spectra and the corresponding gamma distribution. They used the third and sixth moments of the distribution, but in that case the corresponding expressions for  $\mu$  and  $\lambda$  are more complicated. We show in Appendix F that the results do not change much when using  $a_3$  and  $a_6$  to compute the parameters of the gamma distribution.

Although the agreement between simulated size spectra and the gamma distribution turns out to be reasonable, it only works for  $\mu > -1$ . For smaller values of  $\mu$ , the function is no longer normalizable, i.e., the integral over  $f(r) \propto r^\mu$  diverges for  $r \rightarrow 0$  when  $\mu + 1 < 0$ . Most size spectra observed in meteorology have positive values of  $\mu$  [*Naumann and Seifert*, 2016b]. This is mainly because of the effect of evaporation, which is here neglected. Evaporation would lead to a depletion of  $f(r)$  for small values of  $r$  and could lead to spectra that are more typical of a gamma distribution. In our case, we have an approximate  $r^{-1}$  fall-off over nearly two orders of magnitude, followed by an exponential cutoff. This is why the  $\mu$  obtained from the moments turns out to be so close to  $-1$ . Thus, although the usefulness of the gamma distribution is still being debated [*Khain et al.*, 2015], it can actually be remarkably good provided one allows for small negative values of  $\mu$ .

### 3.4 Inhomogeneous collection in a straining flow

Spatial variation in the flow leads to local concentrations and thus to large peak values of  $f(\mathbf{x}, r, t)$  that shorten the collection time  $\tau_{\text{coll}}$  [*Saffman and Turner*, 1956]. Before studying the turbulent case, we consider first collectional growth in a steady two-dimensional (2-D) divergence-free straining flow. The straining flow is numerically inexpensive and easy to control and analyze compared with turbulence.

#### 3.4.1 Pure collection

We consider first the case of pure collection. In Figure 6 we show the time evolution of  $\bar{r}$  for the swarm model with collection scheme II at different grid resolutions ranging from  $64^2$  to  $256^2$  meshpoints. Surprisingly,  $\bar{r}$  grows more slowly as we increase the mesh resolution of the swarm model. Given that the swarm models seem to converge toward the Eulerian model, we are confronted with the question of what causes the growth of  $\bar{r}$  in the swarm model to slow

**Table 2.** Zeroth moment  $n$  (in units of  $\text{m}^{-3}$ ) together with selected normalized moments  $a_\zeta$  (in  $\mu\text{m}$ ), as well as the resulting parameters  $\mu$  (dimensionless),  $\lambda$  (in  $\mu\text{m}^{-1}$ ), and  $\lambda^{-1}$  (in  $\mu\text{m}$ ) for Run 3C at different times. Here,  $\tilde{t} = 1000 t$ .

$t$	$n$	$a_1$	$a_2$	$a_3$	$a_6$	$a_{12}$	$a_{24}$	$\mu$	$\lambda$	$\lambda^{-1}$
0	$10^{11}$	10.2	10.4	10.6	11.3	12.7	16.2	23.61	2.412	0.4
1	$2 \times 10^{10}$	13.0	15.0	18.1	32.4	57.0	87.6	2.16	0.242	4.1
2	$3.8 \times 10^8$	17.7	36.5	68.3	168.0	325.9	530.2	-0.69	0.017	58
3	$1.1 \times 10^7$	29.3	106.7	221.3	562.4	1052.9	1560.7	-0.92	0.003	360

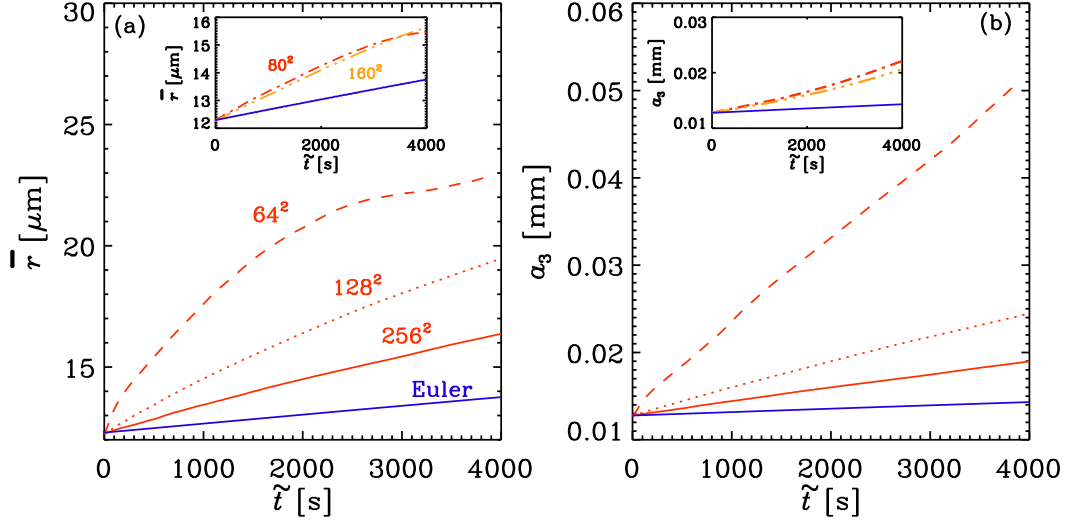


**Figure 6.** Comparison of the evolution of (a) the mean particle size and (b)  $a_3$  in a straining flow for simulations with the swarm approach at different grid resolutions. Here, pure collection with CIC particle interpolation algorithm has been used. The total number of swarms is  $N_p = 300,000$  while  $D_p = 0.05 \text{ m}^2/\text{s}$  and  $\nu_p = 0.01 \text{ m}^2/\text{s}$  are adopted in the Eulerian model. The inset shows the case with NGP mapping instead of the CIC first order interpolation for particle properties. See Runs 7A, 7B, 7C, 7D, 7E, and 7F of Table 1 for simulation details.

down at higher mesh resolution. In this connection, we must emphasize that by default we use the CIC algorithm to evaluate the gas properties at the position of each Lagrangian particle. As explained in section 2.6, the position of the shepherd particle has no purpose other than to determine in which grid cell the swarm resides. It is therefore *not* better to use any kind of interpolation in determining the value of the fluid variables at the position of the swarm, but rather to use NGP mapping. This will play an important role, as will be discussed now. For the sake of solving equations (7) and (8), the use of the CIC algorithm is perfectly valid, but this would only be relevant for a direct Lagrangian tracking algorithm. This can be understood by realizing that in the special case of particles with vanishingly small inertia, the particles will follow their local fluid cell, and hence, two particles will in the real world never collide. However, if the CIC scheme is used for equations (7) and (8), two swarms residing at different positions within the *same* grid cell may have different velocities, and hence, equation (13) may yield a collection.

Since the swarms are filling the entire volume of the grid cell, this means that the two swarms will have different velocities and exist in the same volume, and hence, the swarms may collide. The larger grid cells yield potentially larger velocity differences between the particles, which explains why the collectional growth is larger for the coarser resolutions. When NGP mapping is adopted, the artificial speedup disappears, as shown in the inset of Figure 6.

However, the discrepancy between Lagrangian and Eulerian particle descriptions is still strong for collectional growth in the straining flow as shown in the inset of Figure 6. This is because that in a steady flow, the particles will end up near the vertices of converging flow vectors and will therefore be much more concentrated in the swarm model than what is possible to represent in the Eulerian model. This is evident by comparing the distribution of superparticles belonging to a certain radius (here  $128 \mu\text{m}$ ) with the corresponding distribution function in the Eulerian model; see Figure 7.

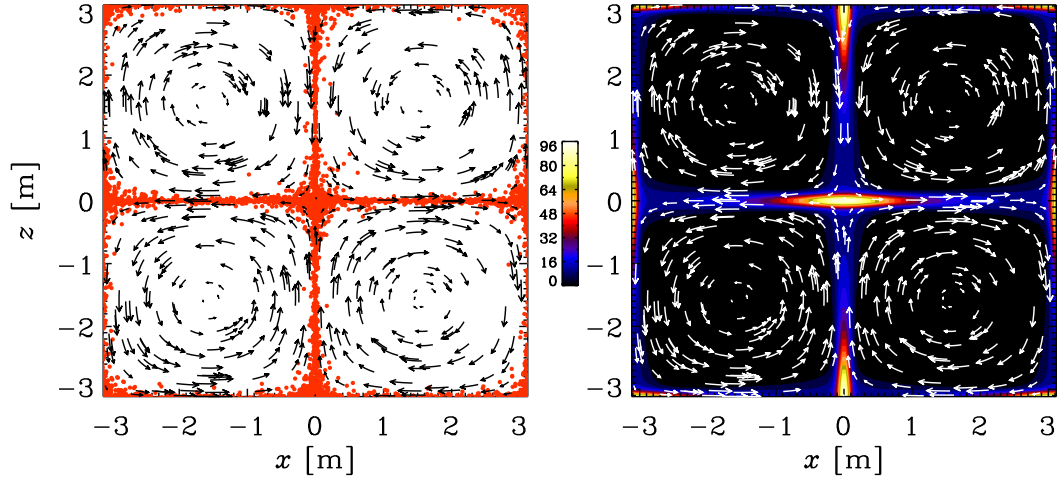


**Figure 7.** Visualization of flow and particle field ( $\bar{t}=1000$  s) in a straining flow for simulations with the swarm approach (left panel; red dotted curve in Figure. 6) and Eulerian approach (right-hand panel; blue curve in Figure. 6). Here the radius of the particles is  $r=128\ \mu\text{m}$ . The swarms are represented by the red dots in the left-hand panel. The contour map shows the spatial distribution of the number density in the right panel. The black and white arrows represent the velocity vectors of the straining flow.

### 3.4.2 Combined condensation and collection

When both condensation and collection play a role, it is no longer possible to define a unique timescale, and the solution depends on both  $\tau_{\text{cond}}$  and  $\tau_{\text{coll}}$ . We consider here the straining flow using  $r_{\text{ini}} = 12\ \mu\text{m}$ ,  $G = 5 \times 10^{-11}\ \text{m}^2/\text{s}$  and  $s = 0.01$ , which yields  $\tau_{\text{cond}} = 144$  s. We investigate the role that particle viscosity and Brownian diffusion play in simulations using the Eulerian model. The Brownian motion of the particles is usually small, so the particle diffusion coefficient  $D_p$  in equation (26) should be finite, but small. Since it is assumed that the particle flows are relatively dilute, there should be very little interaction between the different particle fluids, except for the occasional collections. This implies that the particle viscosity  $\nu_p$  in equation (36) should be close to zero<sup>3</sup>. For the Smoluchowski approach, both  $\nu_p$  and  $D_p$  have to be made large in order to stabilize the simulations in spatially extended cases. It turns out that the values of these diffusion coefficients have a surprisingly strong effect on the solutions, which is shown in Figure 8. This could be due to the fact that the viscosity between the particle fluids diffuses the momentum of the particles and thereby modifies the collection rate.

Comparing now with the swarm approach, which avoids artificial viscosity and enhanced Brownian diffusion altogether, we see from Figure 8 that Eulerian and Lagrangian approaches agree with each other at early times ( $t < 1000$  s). After 1000 s, both swarm and the Eulerian models follow the same trend in the sense that the evolution of  $\bar{r}$  shows a bump. The bump occurs earlier for the swarm model than the Eulerian model. In the extreme case that the artificial viscosity in the Eulerian model were zero, the evolution of  $\bar{r}$ , as obtained from the swarm model, may come closer that of the Eulerian model. However, owing to the absence of a pressure term for particles, discontinuities would develop in the Eulerian model that destabilize the code if the viscosity and Brownian diffusion are too small. Again, this may

<sup>3</sup> Note that the particle viscosity represents the coupling between the particle fluids – not the drag coupling between the particles and the gas phase.

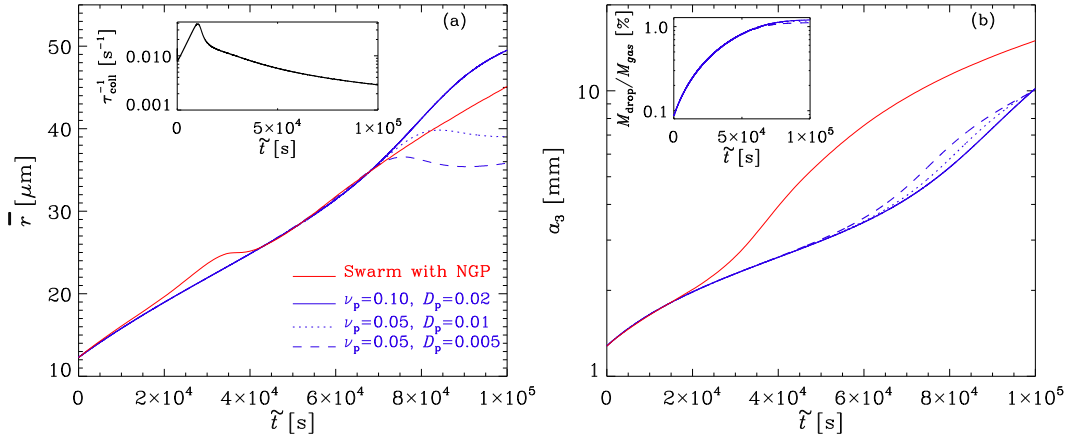


**Figure 8.** Evolution of (a)  $\bar{r}$  and (b)  $a_3$  in the straining flow with combined condensation and collection. The different blue lines correspond to different amounts of artificial viscosity and enhanced Brownian diffusivity. The inset of (a) shows the evolution of the inverse collection timescale  $\tau_{\text{coll}}^{-1}$ . The inset of (b) shows the evolution of the mass ratio. The monotonic growth of the mass ratio demonstrates that particles have not yet populated at the largest mass bin. The initial mean radius, supersaturation, and condensation parameter is given by  $r_{\text{ini}}=12\ \mu\text{m}$ ,  $s=0.01$ , and  $G = 5 \times 10^{-11}\ \text{m}^2/\text{s}$ , respectively, and  $k_{\text{max}}=53$  with  $\beta=2$ . See Runs 9A, 9B, 9C, 9D, and 9E of Table 1 for simulation details.

be a strong argument in favor of using the swarm model for studying the collectional growth of cloud droplets.

To relate the speed of evolution in Figure 8 to  $\tilde{\tau}_{\text{coll}}$ , we plot in the inset of panel (a) the inverse of its unscaled value,  $\tau_{\text{coll}}$ , as a function of time. On average, we have  $\tau_{\text{coll}} \approx 100$ . It is comparable to  $\tau_{\text{cond}} = 144\ \text{s}$  and both are long compared with  $\tau_{\text{cor}} \approx 1.4$ . The relevant quantity is the scaled value,  $\tilde{\tau}_{\text{coll}}$ , which is much larger  $\approx 10,000$ . This may suggest that the speed of growth is not governed by the spatially averaged kernel, but by its value weighted toward regions where the concentration is high.

We recall that growth of cloud droplets driven by pure collections in the straining flow depends on the models (Eulerian and Lagrangian models; see detailed comparisons in section 3.4.1). This suggests that condensation has a “regularizing” effect in that it makes the overall evolution of  $\bar{r}$  much less dependent on the initial conditions and other model details. This is due to the fact that the condensation process with constant positive supersaturation value leads to narrow size spectra of cloud droplets.

Another interesting aspect is the bump in the evolution of the mean radius. At first glance it seems counterintuitive that  $\bar{r}$  can actually decrease during some time interval. In Appendix G we consider an example of four particles, two large ones and two small ones. If two small ones collide, we still have the two large ones, but only 3 particles in total after the collection, so the average radius increases from  $1/2$  to  $2/3$ . On the other hand, if two large ones collide, we are still left with the two small ones and one particle whose radius has only grown by a factor of  $2^{1/3} \approx 1.26$  (the radius scales with the mass to the  $1/3$  power). The average radius is therefore  $2^{1/3}/3 \approx 0.42$ , which is less than the original mean radius, which is half the radius of the large ones.

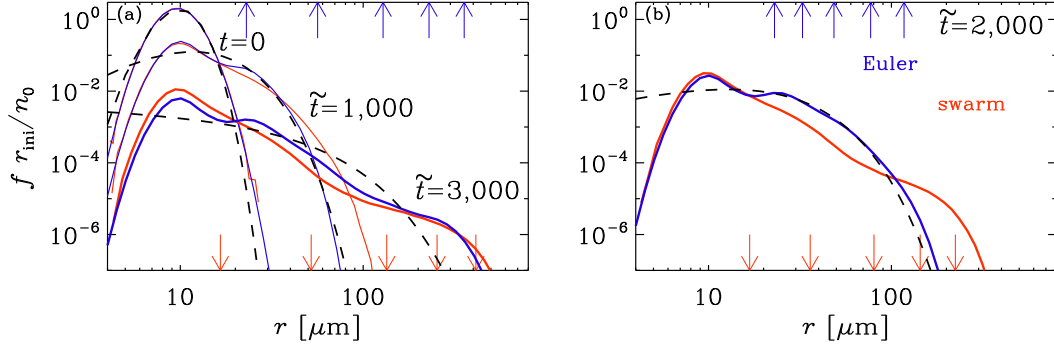


**Figure 9.** Comparison of size spectra for Lagrangian (red lines) and Eulerian (blue lines) approaches at different times in the presence of 2-D turbulence and no gravity nor condensation. The arrows show the values of different moments ( $a_1$ ,  $a_3$ ,  $a_6$ ,  $a_{12}$ , and  $a_{24}$ , from left to right) of the size spectra at time (a)  $\tilde{t} = 3000$  s and (b)  $\tilde{t} = 2000$  s. The largest departure between both approaches occurs for  $\tilde{t} = 2000$  s and is plotted separately in the right-hand panel. The black dashed curves are the fitted gamma distribution of the Eulerian model. See Runs 10A and 10B of Table 1 for simulation details.

### 3.5 Growth of droplets in 2-D turbulence

Turbulence is generally believed to help bridging the size gaps in both cloud droplet and planetesimal formation. In this section, pure turbulence-generated collections are simulated using both the Eulerian and Lagrangian models. We consider a 2-D squared domain of side length  $L = 0.5$  m at a resolution of 512<sup>2</sup> meshpoints, with viscosity  $\nu = 5 \times 10^{-4}$  m<sup>2</sup> s<sup>-1</sup> (which is about 50 times the physical value for air), average forcing wavenumber  $k_f \approx 40$  m<sup>-1</sup>, i.e.,  $k_f L / 2\pi \approx 3$ , and a root-mean-square velocity  $u_{\text{rms}} = 0.8$  m s<sup>-1</sup>, resulting in a Reynolds number of  $\text{Re} = u_{\text{rms}} / \nu k_f \approx 40$ . Our choice of  $k_f L / 2\pi \approx 3$  corresponds to forcing at large scales that are not yet too large to be affected by constraints resulting from the Cartesian geometry. The rate of energy dissipation per unit volume is  $\epsilon = 2\nu \langle \mathbf{S}^2 \rangle \approx 0.1$  m<sup>2</sup> s<sup>-3</sup> and the turnover time is  $\tau_{\text{to}} = (u_{\text{rms}} k_f)^{-1} \approx 0.03$  s. For the Lagrangian model, we use NGP mapping while for the Eulerian model we adopt artificial viscosity and enhanced Brownian diffusivity for the particles ( $\nu_p = D_p = 10^{-3}$  m<sup>2</sup> s<sup>-1</sup>).

#### 3.5.1 Size spectra

Figure 9 shows the comparison of size spectra for the swarm and Eulerian models in 2-D turbulence. The agreement of the spectra as well as the high moments for both schemes is good. Except for the latest time, the corresponding gamma distribution agrees reasonably well with the simulated size spectra, as shown by the black dashed curves in Figure 9; see selected moments and the parameters for the corresponding gamma distribution in Table 3. Here we also give the parameters  $\mu$  and  $\lambda^{-1}$  of the corresponding gamma distribution. Again,  $\mu$  becomes negative at the last time, but, unlike the case with pure gravity (Table 2), its value is still far away from  $-1$ . Furthermore,  $\lambda^{-1}$  is now 10 times smaller than  $a_{24}$  and does therefore not represent the maximum droplet radius.

We recall that good agreement is also observed in the case with gravity. Hence, we conclude that the gamma distribution can reasonably well represent the collectional size spectra. This may provide a strong argument in favor of using the gamma distribution when modelling cloud microphysics.

**Table 3.** Similar to Table 2, but now for Run 10A with turbulence and no gravity. Here,  $\tilde{t} = 100 t$ .

$t$	$n$	$a_1$	$a_2$	$a_3$	$a_6$	$a_{12}$	$a_{24}$	$\mu$	$\lambda$	$\lambda^{-1}$
0	$10^{10}$	10.2	10.4	10.6	11.3	12.7	16.2	23.42	2.394	0.4
10	$2.0 \times 10^9$	15.0	16.6	18.3	23.3	31.4	43.1	3.50	0.300	3.3
20	$3.4 \times 10^8$	23.0	27.6	32.6	48.1	75.6	115.0	1.25	0.098	10
30	$6.7 \times 10^7$	22.8	34.7	56.4	132.2	243.2	388.0	-0.23	0.034	30

### 3.5.2 Other numerical aspects

It is worth noting that the MBR convergence of the Smoluchowski equation depends on the flow pattern. While gravitational collection is rather sensitive to MBR (see Appendix E), it is much less sensitive for the straining flow and converges at  $k_{\max} \approx 55$  in turbulence.

We emphasize that for the swarm model, the interpolation scheme of the tracked swarms does affect the results, but this does not seem to be the case for turbulence. Turbulence continues to mix particles all the time while the straining flow tends to sweep up particles into predetermined locations that do not change. We may therefore conclude that the restriction on the interpolation scheme depends on the spatio-temporal properties of the flow. Nevertheless, a high-order interpolation is not strictly applicable to the swarm model.

It is worth noting that in the case with pure gravity, the Eulerian model is rather sensitive to the presence or absence of the  $\mathcal{M}_k$  term. This is neither the case for turbulence nor for the straining flow as will be discussed in Appendix B.

### 3.5.3 Comparison of computational cost

Comparing the Lagrangian and Eulerian models in Figure 9, it is worth noting that the Lagrangian one is clearly superior to the Eulerian one in terms of CPU time for simulating the collectional process in 2-D turbulence. A similar conclusion was drawn by *Shima et al.* [2009], who found the Lagrangian model to be computationally faster than the Eulerian one. We compare the computational cost between Eulerian and Lagrangian models using the 2-D turbulence runs 10A and 10B (runs in Figure 9), which have comparable accuracy; see Table 1 for details of these runs. The Lagrangian model with  $1.2 \times 10^6$  superparticles covers 217 s in physical time within 24 hours of wall-clock time on 512 CPUs, while the Eulerian model with 53 mass bins covers only 48 s in physical time within 24 hours wall-clock time on 1024 CPUs. This example demonstrates that the Lagrangian model is roughly ten times more efficient than a comparable Eulerian one.

### 3.5.4 Combined condensation and collection

The combined condensational and collectional growth in turbulence is investigated as well. Again, the results are similar to the case with pure collectional growth due to the fact that the condensation process in the present study with constant supersaturation is homogeneous. In future studies, the supersaturation should be calculated self-consistently and the effects of turbulence on the condensational growth should be considered, similar to what was done previously [*Kumar et al.*, 2014; *Sardina et al.*, 2015].

## 4 Conclusion

The combined collectional and condensational growth of cloud droplets is studied in numerical simulations where the gas phase is solved on a mesh, while the particle phase is

approximated by a point particle approach and is treated either by an Eulerian or a Lagrangian formalism. It is found that the Lagrangian approach agrees well with the analytic solution of condensational growth. By contrast, the Eulerian approach requires high resolution in the number of mass bins to avoid artificial speedup of the growth rate, which agrees with previous findings [Ohtsuki *et al.*, 1990; Drajzkowska *et al.*, 2014]. It is worth noting that the MBR dependency is closely related to the temporal and spatial properties of the flow. The dependency is strongest for gravity [ $\mathbf{u} = \mathbf{0}$  in equation (1)], less strongly for the straining flow, and weak for turbulence.

A detailed comparison of the collectional size spectra between the Lagrangian and Eulerian models demonstrates consistency between the two, especially when both condensation and collection are included. This suggests that condensation has a regularizing effect and makes the overall evolution of the mean radius less dependent on details such as the precise form of the initial condition or discretization errors that might affect the early evolution. However, the evolution of the mean radius, i.e., the ratio of the two lowest (first and zeroth) moments of the size distribution function, is a rather insensitive measure of particle growth. This is also seen in the fact that the mean particle radius often increases by not much more than a factor of three, while the size distribution can become rather broad and even millimeter-sized particles can be produced within a relatively short time. The mean particle radius is also not the most relevant diagnostics in that it does not characterize properly the growth of the largest particles. In fact, as we have shown in Appendix G, the mean radius actually *decreases* when two large particles collide. This is somewhat counterintuitive, but actually quite natural. When two very small particles collide, the sum of all radii does basically not change, but the number of particles decreased by one, so the average increases. By contrast, when two large particles collide, the particle number again decreases by one, but the sum of the radii decreases from 2 to  $2^{1/3} \approx 1.26$ , so the average also decreases.

Remarkably, we found that the simulated tails of the size spectra agree fairly well with those obtained from the gamma distribution for negative  $\mu$ . More importantly, the agreement is good both for gravity and turbulence cases.

When studying pure collection, the Eulerian approach yields satisfactory results only when the mass bins are sufficiently fine. Furthermore, for collections in the case of a straining flow, it is found that the Eulerian approach requires artificially large viscosity and Brownian diffusivity for keeping the resulting shocks in the particle fluid resolved. Because of this, it seems that for future studies of the effect of turbulence on condensational and collectional growth of particles, the Lagrangian swarm approach would be most suitable. However, several precautions have to be taken. First, the symmetric collection scheme II [Shima *et al.*, 2009] is to be preferred because it shows less scatter in the mean radius than the asymmetric scheme I. This is because in scheme I the particle number is adjusted to keep the total mass in the swarm constant. Second, when interpolation of the gas properties at the position of each Lagrangian particle is invoked (for example the CIC algorithm or the triangular shaped cloud scheme), both collection schemes yield artificially increased collection rates. This is because two swarms within the same grid cell may always collide since the interpolation of the fluid velocity results in a velocity difference between the two swarms. This causes a speedup of the collection rate already at early times. At higher grid resolution, the interpolated velocity differences are smaller, which reduces the collectional growth. Therefore, it is best to map the gas properties to just the nearest grid point, which is found to yield converged results even at low resolution.

A shortcoming of the Eulerian model is that self-collections are strictly impossible. This should be mitigated by using finer mass bins, but it turns out that finer mass bins do not change the collection rate at early times, but rather decrease it at later times. This indicates that the contribution of self-collections to the collection rate is relatively small; see Appendix H for details.

The discrepancy between Lagrangian and Eulerian particle descriptions is particularly strong in the time-independent straining flow. This is because particles tend to be swept into extremely narrow lanes, which leads to high concentrations that can never be achieved with the Eulerian approach, in which sharp gradients must be smeared out by invoking artificial viscosity and large Brownian diffusivity. On the other hand, we are here primarily interested in turbulent flows that are always time-dependent, which limits the amount of particle concentration that can be achieved in a given time. In that case, the discrepancies between Eulerian and Lagrangian approaches are smaller at early times, but there are still differences in the evolution of the mean radius at late times. This can easily be caused by changes in the relative importance of collections of large and small particles. This is confirmed by the fact that the size distribution spectra in the turbulent case are more similar for Lagrangian and Eulerian approaches than in the straining flow.

Our present work neglects local and temporal changes in the supersaturation. In future studies, we will take into account that the supersaturation increases (decreases) as a fluid parcel rises (falls) and that droplet condensation (evaporation) act as sinks (sources) of supersaturation. We would then be able to account for the fact that the total water content should remain constant and that the supersaturation would become progressively more limited as water droplets grow by condensation. Another important shortcoming is our assumption of perfect collection efficiency, which resulted in artificially rapid cloud droplets growth. Alleviating these restrictions will be important tasks for future work. Furthermore, we have here only considered 2-D turbulence. Extending our work to 3-D is straightforward, but our conclusions regarding the comparison of different schemes should carry over to 3-D.

## Acknowledgments

We thank Nathan Kleeorin, Dhruvadya Mitra, and Igor Rogachevskii for useful discussions. We also thank the anonymous referees for constructive comments and suggestions that lead to substantial improvements in the manuscript. This work was supported through the FRINATEK grant 231444 under the Research Council of Norway, the Swedish Research Council grant 2012-5797, and the grant “Bottlenecks for particle growth in turbulent aerosols” from the Knut and Alice Wallenberg Foundation, Dnr. KAW 2014.0048. The simulations were performed using resources provided by the Swedish National Infrastructure for Computing (SNIC) at the Royal Institute of Technology in Stockholm. This work utilized the Janus supercomputer, which is supported by the National Science Foundation (award number CNS-0821794), the University of Colorado Boulder, the University of Colorado Denver, and the National Center for Atmospheric Research. The Janus supercomputer is operated by the University of Colorado Boulder. The source code used for the simulations of this study, the PENCIL CODE, is freely available on <https://github.com/pencil-code/>. The input files as well as some of the output files of the simulations listed in Table 1 are available under [http://www.nordita.org/~brandenb/projects/SwarmSmolu\\_numerics/](http://www.nordita.org/~brandenb/projects/SwarmSmolu_numerics/).

# Appendices

## A Upwinding scheme for a nonuniform mesh

In the presence of condensation alone, the evolution equation for  $f(r, t)$  as a function of radius  $r$  and time  $t$  is given by

$$\frac{\partial f}{\partial t} = -\frac{\partial}{\partial r}(fC), \quad (\text{A.1})$$

where  $C \equiv dr/dt$  and is given by equation (6). Thus, we have

$$\frac{\partial f}{\partial t} = -A \frac{\partial}{\partial r} \left( \frac{f}{r} \right) \quad (\text{A.2})$$

where  $A = Gs$  is assumed independent of  $r$ ; see equation (13.14) of *Seinfeld and Pandis* [2006]. It can be seen from the form of the analytic solution that there will be a discontinuity at  $r^2 = 2At$ , which is numerically difficult to handle. In particular, it is difficult to ensure the positivity of  $f$ . For these reasons, a low-order upwind scheme is advantageous. Furthermore, expanding the RHS of equation (A.2) using the quotient rule,

$$\frac{\partial f}{\partial t} = \frac{A}{r^2}f - \frac{A}{r} \frac{\partial f}{\partial r}, \quad (\text{A.3})$$

it is obvious that the first term in isolation would lead to exponential growth of  $f$  proportional to  $\exp(At/r^2)$ , which must be partially canceled by the second term. If the cancellation is numerically imperfect,  $f(r, t)$  will indeed grow exponentially, which tends to occur in regions where  $r^2 < 2At$ , i.e., where  $f$  should vanish. For nonuniform mesh spacing,  $r_k$  with  $k = 1, 2, \dots, k_{\max}$ , the first-order upwind scheme can be written as

$$\frac{\partial f_k}{\partial t} = c_k^+ \frac{f_{k+1}}{r_{k+1}} + c_k^0 \frac{f_k}{r_k} + c_k^- \frac{f_{k-1}}{r_{k-1}} \quad (\text{A.4})$$

with

$$c_k^\pm = \pm \frac{1}{2} \frac{|A| \mp A}{r_{k\pm 1} - r_k}, \quad c_k^0 = -c_k^+ - c_k^-. \quad (\text{A.5})$$

On the boundaries of the radius bins at  $k = 1$  and  $k_{\max}$ , equation (A.4) cannot be used unless we make an assumption about the nonexistent points outside the interval  $1 \leq k \leq k_{\max}$ . For example, for  $k = k_{\max}$ , the coefficient  $c_k^+$  would multiply  $f_{k+1}/r_{k+1}$ , which is not defined. Therefore, a simple assumption is to set  $c_k^+ = 0$ . However,  $c_k^+$  also enters in the expression for  $c_k^0$ , which is the factor in front of  $f_k/a_k$ . The coefficient  $c_k^+$  can only be nonvanishing when  $A < 0$ . If we were to omit  $c_k^+$  in the expression for  $c_k^0$ , then, for  $A < 0$ , the value of  $f_k$  would not evolve at  $k = k_{\max}$  and would be frozen. Thus, the non-existing points lead to an unphysical situation. It would be natural to assume that at  $k = k_{\max}$ ,  $f_k$  should decay with time at a rate  $-(|A| - A)/r_k$ . Therefore, assume

$$c_k^+ = 0, \quad c_k^0 = -(|A| - A)/r_k - c_k^- \quad (\text{for } k = k_{\max}) \quad (\text{A.6})$$

and  $c_k^-$  unchanged, and analogously

$$c_k^- = 0, \quad c_k^0 = -(|A| + A)/r_k - c_k^+ \quad (\text{for } k = 0) \quad (\text{A.7})$$

and  $c_k^+$  unchanged.

## B Momentum conservation solution of the Eulerian model

The purpose of this appendix is to derive the momentum-conserving velocity kick  $\mathcal{M}_k$  in equation (35) and to demonstrate how it works. Each collection event involves three partners, which we denote by subscripts  $i$ ,  $j$ , and  $k$ , where  $k$  is the result of the collection between  $i$  and  $j$ . Mass conservation implies that  $f_i m_i + f_j m_j + f_k m_k$  is constant, i.e., its time derivative vanishes. Likewise, momentum conservation implies that

$$\frac{\partial}{\partial t} (f_i m_i \mathbf{v}_i + f_j m_j \mathbf{v}_j + f_k m_k \mathbf{v}_k) = 0. \quad (\text{B.1})$$

The time derivatives of  $f$  caused by collections is  $\mathcal{T}$ , while that of  $\mathbf{v}$  is  $\mathcal{M}$ . However, only the resulting particle  $k$  will suffer a kick, while  $i$  and  $j$  do not, so we have

$$\mathcal{T}_i m_i \mathbf{v}_i + \mathcal{T}_j m_j \mathbf{v}_j + \mathcal{T}_k m_k \mathbf{v}_k + f_k m_k \mathcal{M}_k = 0. \quad (\text{B.2})$$

As seen from equation (33), for the collection of  $i$  and  $j$ , the increase in  $f_k$  is given by

$$\mathcal{T}_k = K_{ij} f_i f_j \frac{m_i + m_j}{m_k}, \quad (\text{B.3})$$

**Table B.1.** Total particle momentum in  $\text{kgm}^{-2}\text{s}^{-1}$  after three different times using the Eulerian model.

case	$\mathcal{T}$	$\mathcal{M}$	$g$	$t = 0.0 \text{ s}$	$t = 0.1 \text{ s}$	$t = 1 \text{ s}$	$t = 10 \text{ s}$
A	0	0	0	0.8042	0.8042	0.8042	0.8042
B	$\neq 0$	0	0	–	0.3386	0.0012	0.00
C	$\neq 0$	$\neq 0$	0	–	0.8035	0.8032	0.75
D	0	0	$\neq 0$	–	0.3070	–4.1679	–48.92
E	$\neq 0$	0	$\neq 0$	–	–0.1586	–4.9709	–49.72
F	$\neq 0$	$\neq 0$	$\neq 0$	–	0.3063	–4.1673	–45.51

The initial parameters are:  $v_1=1 \text{ m s}^{-1}$  and  $v_2=2 \text{ m s}^{-1}$  at radius bins  $r_1=100 \mu\text{m}$  and  $r_2=112 \mu\text{m}$  ( $\times 2^{1/6}$  larger) with  $n_0=10^8 \text{ m}^{-3}$  distributed evenly over the first two mass bins.

while the corresponding decreases in both  $f_i$  and  $f_j$  are

$$\mathcal{T}_i = \mathcal{T}_j = -K_{ij}f_i f_j, \quad (\text{B.4})$$

which evidently obeys mass conservation, i.e.,  $\mathcal{T}_i m_i + \mathcal{T}_j m_j + \mathcal{T}_k m_k = 0$ . Inserting equations (B.3) and (B.4) into equation (B.2) and solving for  $\mathcal{M}_k$  yields

$$\mathcal{M}_k = \frac{1}{f_k m_k} K_{ij} f_i f_j [m_i v_i + m_j v_j - (m_i + m_j) v_k]. \quad (\text{B.5})$$

We give in Table B.1 the values of the total momentum of all particles in the Eulerian model,  $\sum \hat{f}_i m_i v_i$ , at three different times for a model without spatial extent (0-D). Initially, we have two mass bins with velocities 1 and 2, which leads to collectional growth if  $\mathcal{T} \neq 0$ . Drag with the gas is here neglected. In the absence of gravity, the total momentum is the same for all three times when there is no collection ( $\mathcal{T} = 0$ ). For  $\mathcal{T} \neq 0$ , there is a dramatic change of momentum if the  $\mathcal{M}$  term is neglected (case B). With the  $\mathcal{M}$  term included, momentum is reasonably well conserved (compare case C with case A). In the presence of gravity, the momentum changes just because of gravitational acceleration (cases D–F). However, we would not expect the total momentum to change dramatically when we allow for collection ( $\mathcal{T} \neq 0$ ). We see that without the  $\mathcal{M}$  term the total momentum departs significantly from the case without collection (case E), while with the  $\mathcal{M}$  term included, the values of total momentum are similar to those without collection (compare case F with case D). This validates the implementation of the momentum conserving term.

Let us now discuss the effect of the momentum conserving correction in the context of gravitational collection. This is shown in Figure B.1, where we compare size spectra for  $\beta = 2$  and 8 with and without the  $\mathcal{M}$  term. It turns out that without the  $\mathcal{M}$  term, the growth of large droplets is increased when the MBR is large ( $\beta = 8$ ). This is not the case, however, when the  $\mathcal{M}$  term is included, which leads to a much slower growth of the largest droplets. On the other hand, as demonstrated above, the  $\mathcal{M}$  term leads to a decrease of the momentum of the large droplets, which explains the absence of particles above 1 mm at  $\tilde{t} = 3000 \text{ s}$  and the increase at smaller radii.

Remarkably, in turbulence, the evolution of the size spectra are almost the same with or without momentum correction term. This is shown in Figure B.2. It is still unclear why the effect of the momentum correction term depends so strongly on the flow pattern. Further investigation is required to understand this in the future work. However, one might speculate that the momentum conservation correction accumulates numerical errors with increasing number of mass bins, so it is unclear that this procedure leads to more accurate results.

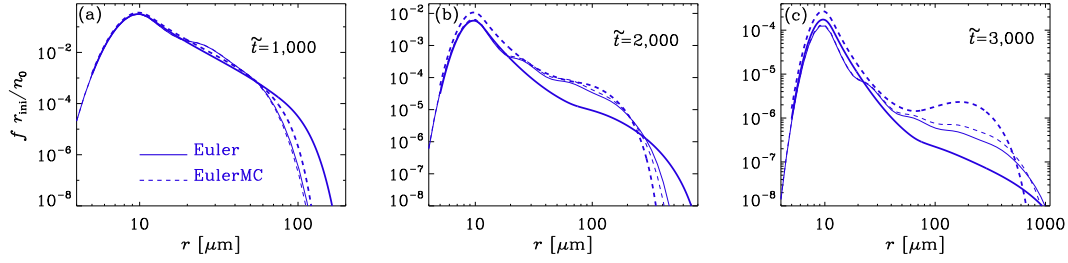


**Figure B.1.** Same as Figure 3, but with the Eulerian model with momentum conservation (blue dashed lines, denoted by “EulerMC”) included. Here we only compare EulerMC and Euler. Thick lines:  $\beta = 8$ ; thin lines:  $\beta = 2$ . See additional Runs 3A, 3D, and 3E in Table B.2 for simulation details.

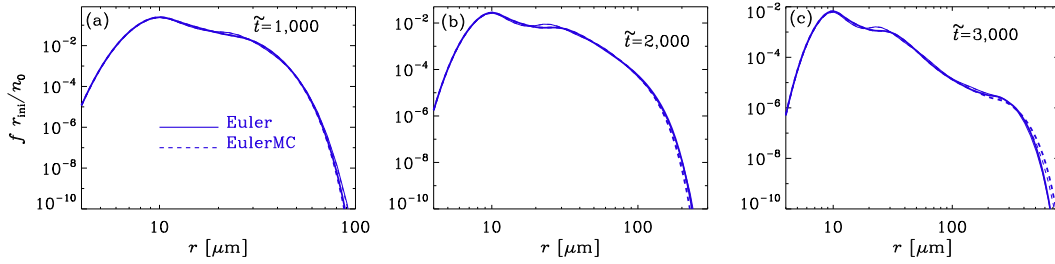


**Figure B.2.** The effect of the momentum conserving term for a turbulent flow (dashed lines, denoted by “EulerMC”) compared with the case without it (denoted by “Euler”), same as in Figure 9. Thick lines:  $\beta = 8$ ; thin lines:  $\beta = 2$ . See additional Runs 10C, 10D, and 10E in Table B.2 for simulation details.

### C MBR dependency for condensation

As discussed in section 3.1, one needs extremely large MBR to model condensation accurately. This becomes particularly critical when using logarithmic spacing on a mesh with small values of  $\delta$ . The purpose of this appendix is to demonstrate the effects on the tails of the distribution. In Figure C.1 we show  $(a_{24}/r_{\text{ini}})^2$  for different MBR ( $\beta$ ) and compare with  $(\bar{r}/r_{\text{ini}})^2$ . In the Eulerian model, we consider the values  $\beta = 2, 8, \text{ and } 128$  over the mass bin interval  $2\text{--}20\ \mu\text{m}$ , so the number of bins are  $k_{\text{max}} - 1 = 20, 80, \text{ and } 1280$ , respectively. In the Lagrangian model, we use  $N_p = 10,000$  and  $N_{\text{grid}} = 16^3$ , so  $N_p/N_{\text{grid}} \approx 2.4$ . At higher MBR, the  $a_\zeta$  for different values of  $\zeta$  converge to the same value, but not at low MBR (see the inset of the first panel). This can have a lasting effect on the growth of the higher moments in the sense that the slope in Figure C.1 is increased at all later times. This is consistent with earlier findings [Ohtsuki *et al.*, 1990; Drązkowska *et al.*, 2014]. When collection is included, the artificially broadened tails in the distribution can be particularly dangerous, because they would have a strong effect on the rate of collection, which would be faster when the  $a_\zeta$  for large values of  $\zeta$  are increased by the artificially broadened size distribution. In the right hand-panel of Figure C.1, we compare  $(a_{24}/r_{\text{ini}})^2$  for both the swarm model and the high MBR Eulerian simulation. The inset shows for both the swarm and the Eulerian models the departure,

$$\Delta[(a_{24}/r_{\text{ini}})^2] = (a_{24}/r_{\text{ini}})^2 - (a_{24}/r_{\text{ini}})^2_{\text{analyt}}, \quad (\text{C.1})$$

from the analytic solution. We see that at late times the swarm model agrees perfectly, while the Eulerian one shows small but persistent departures, as mentioned before. From this it is clear that the swarm model reproduces the high MBR Eulerian simulation rather accurately, but at a much lower computational cost.

**Table B.2.** Summary of additional simulations presented in the appendix.

Run	Scheme	Dim	$L$ (m)	$N_p$	$N_{\text{grid}}$	IM	Processes	$\beta$	$n_0$ (m <sup>-3</sup> )	Flow	$D_p$ (m <sup>2</sup> /s)	$\nu_p$ (m <sup>2</sup> /s)
1B	Eu	0-D	0.5	–	–	–	Con	2	10 <sup>8</sup>	–		
2A	Eu	0-D	0.5	–	–	–	Con	8	10 <sup>8</sup>	–		
3A	Eu	0-D	0.5	–	–	–	Col	2	10 <sup>8</sup>	grav		
3B	Eu	0-D	0.5	–	–	–	Col	32	10 <sup>8</sup>	grav		
3D	EuMC	0-D	0.5	–	–	–	Col	2	10 <sup>10</sup>	grav		
3E	EuMC	0-D	0.5	–	–	–	Col	128	10 <sup>11</sup>	grav		
4A	SwI	3-D	0.5	$2N_{\text{grid}}$	$32^3$	CIC	Col	–	10 <sup>10</sup>	grav		
4C	SwI	3-D	0.5	$8N_{\text{grid}}$	$32^3$	CIC	Col	–	10 <sup>10</sup>	grav		
4D	SwII	3-D	0.5	$2N_{\text{grid}}$	$32^3$	CIC	Col	–	10 <sup>10</sup>	grav		
4E	SwII	3-D	0.5	$4N_{\text{grid}}$	$32^3$	CIC	Col	–	10 <sup>10</sup>	grav		
4F	SwII	3-D	0.5	$8N_{\text{grid}}$	$32^3$	CIC	Col	–	10 <sup>10</sup>	grav		
4G	SwI	3-D	0.5	$4N_{\text{grid}}$	$32^3$	CIC	Col	–	10 <sup>10</sup>	grav		
5A	SwII	3-D	0.5	$2 \times 10^3$	$N_p/4$	CIC	Col	–	10 <sup>10</sup>	grav		
5B	SwII	3-D	0.5	$16 \times 10^3$	$N_p/4$	CIC	Col	–	10 <sup>10</sup>	grav		
5C	SwII	3-D	0.5	$442 \times 10^3$	$N_p/4$	CIC	Col	–	10 <sup>10</sup>	grav		
5D	SwII	3-D	0.5	$1024 \times 10^3$	$N_p/4$	CIC	Col	–	10 <sup>10</sup>	grav		
8A	Eu	2-D	$2\pi$	–	$80^2$	–	Col	2	10 <sup>10</sup>	strain	0.01	0.05
8B	Eu	2-D	$2\pi$	–	$80^2$	–	Sym	2	10 <sup>10</sup>	strain	0.01	0.05
8C	Eu	2-D	$2\pi$	–	$80^2$	–	Ave	2	10 <sup>10</sup>	strain	0.01	0.05
8D	Eu	2-D	$2\pi$	–	$80^2$	–	Sym	4	10 <sup>10</sup>	strain	0.01	0.05
8E	SwII	2-D	$2\pi$	$5 \times 10^4$	$80^2$	NGP	Col	–	10 <sup>10</sup>	strain		
8F	Eu	2-D	$2\pi$	–	$80^2$	–	Col	4	10 <sup>10</sup>	strain	0.01	0.05
8G	Eu	2-D	$2\pi$	–	$128^2$	–	Both	4	10 <sup>8</sup>	strain	0.01	0.05
10C	EuMC	2-D	0.5	–	$512^2$	–	Col	2	10 <sup>10</sup>	turb	0.001	0.001
10D	EuMC	2-D	0.5	–	$512^2$	–	Col	4	10 <sup>10</sup>	turb	0.001	0.001
10E	Eu	2-D	0.5	–	$512^2$	–	Col	4	10 <sup>10</sup>	turb	0.001	0.001

Here, the abbreviations are the same as the ones in Table 1 but with additional abbreviations listed below. ‘‘Sym’’ refers to collection with symmetric self-collection invoked in Eulerian model, ‘‘Ave’’ refers to collection with average self-collection invoked in Eulerian model, ‘‘EuMC’’ refers to the Eulerian model with momentum conservation invoked.

## D Statistical convergence of the swarm model

The purpose of this appendix is to investigate the statistical convergence with respect to the number of grid cells and swarms. First we inspect the convergence property of  $N_p/N_{\text{grid}}$ . The simulations have been performed with  $32^3$  grid points and different average numbers of swarm particles per grid point ( $N_p/N_{\text{grid}} = 2-8$ ). It can be seen from the upper panels of Figure C.2 that the swarm simulations with collection scheme II almost converge for  $N_p/N_{\text{grid}} = 4$ . The details of these additional runs are summarized in Table B.2

From the lower panels of Figure C.2 it can be seen that for simulations with  $N_p/N_{\text{grid}} = 4$ , the results are more or less converged when the total number of swarms reaches  $128 \times 10^3$ . Since all fluid variables are spatially uniform in these simulations, the number of grid points has no effect on the fluid. The number of swarms can therefore be changed by increasing the total number of grid points while maintaining  $N_p/N_{\text{grid}} = 4$  (the value of  $n_i$  is approximately the same in all cases;  $n_i \approx 10^9$ ). However, as reported by *Arabas and Ichiro Shima* [2013], when the swarm model is used in an LES simulation, certain macrophysical features of their simulated could field does not show convergence regarding grid resolution.

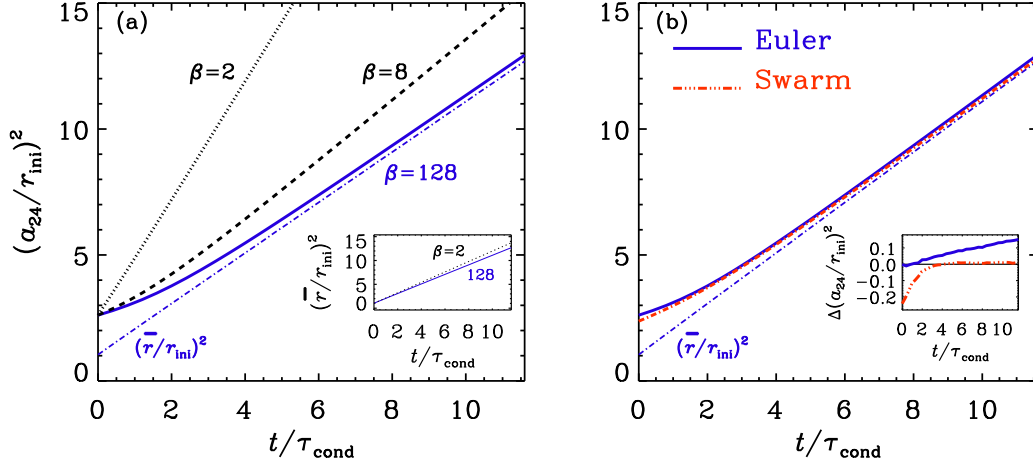


**Figure C.1.** Same run as in Figure 1, but with different  $\beta$  for the Eulerian model. Comparison of the time evolution [in units of  $\tau_{\text{cond}}$ , as given by equation (28)] of  $(a_{24}/r_{\text{ini}})^2$  for  $\beta=2$  (dotted red), 8 (dashed black), and 128 (solid blue) for condensation, together with  $(\bar{r}/r_{\text{ini}})^2$  for  $\beta=128$  (dash-dotted blue) using the mass bin interval  $2\text{--}20\mu\text{m}$ . The inset shows  $(\bar{r}/r_{\text{ini}})^2$  for  $\beta=2$  (dotted red) and 128 (solid black). The right panel shows a comparison of the 24th moment between the Eulerian model with 1281 mass bins (solid blue) and the swarm model with collection scheme I,  $N_p=10,000$ , and  $N_{\text{grid}}=16^3$  (red). The inset shows the difference of the squares to the analytic solution for the Eulerian model (solid blue) and the swarm model (triple-dot-dashed red). Here, the parameters for condensation and the initial conditions are the same as for Figure 1. See additional Runs 1B and 2A of Table B.2 for simulation details.

## E MBR dependency for collection

In Figure E.1, we compare the evolutions of  $\bar{r}$  and  $a_{24}$  using different MBR and thus different values of  $\beta$  for pure collection experiment. We also considered the evolution of  $a_3$  and  $a_6$ , but it was similar to that of  $a_{24}$  in that the Eulerian solutions for different MBR agreed well with each other. For  $\bar{r}$  the evolutions are strongly MBR dependent. Nevertheless, the evolution of  $a_{24}$  with different MBR are similar over a wide range of MBR spanning from  $k_{\text{max}} = 55\text{--}3457$ . We also tested the MBR dependency using a constant kernel. In that case, it turns out that the results converge only for  $k_{\text{max}} \geq 50$ .

## F Gamma distribution from higher moments

The purpose of this appendix is to show that the characterization of size spectra in terms of a gamma distribution is not strongly dependent on whether its parameters are computed based on the moments  $a_1$  and  $a_2$ , as done here, or based on  $a_3$  and  $a_6$ , as done in *Naumann and Seifert* [2016b]. In the former case, equation (44) was used to obtain  $\mu$  as a function of  $a_2/a_1$ , while in the latter  $a_6/a_3$  was used to obtain  $\mu$ . Once  $\mu$  is known,  $\lambda$  can also be obtained. In the following we generalize this approach to arbitrary values of  $\zeta$  for the ratios  $a_\zeta/a_{\zeta/2}$ .

To compute the coefficients for any pair of moments  $a_\zeta$  to  $a_{\zeta/2}$ , we first calculate

$$n a_\zeta^\zeta = \int r^\zeta f(r) dr = \frac{n}{\lambda^\zeta} \frac{\Gamma(\mu + \zeta + 1)}{\Gamma(\mu + 1)}. \quad (\text{F.1})$$

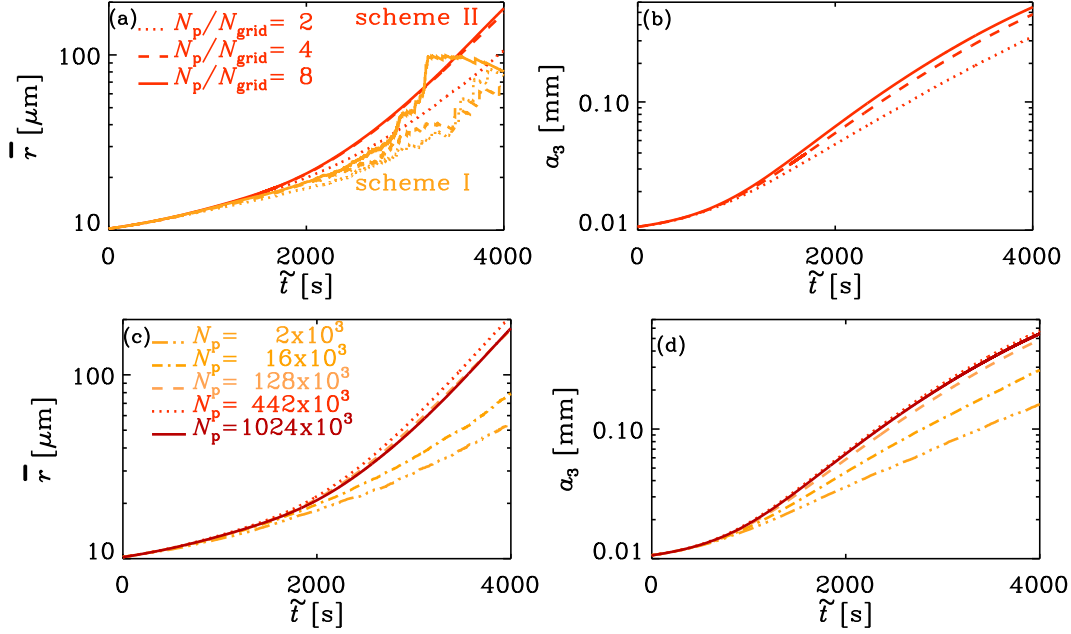


**Figure C.2.** Same as Figure 2, but here we only study the statistical convergence properties of swarm model. Upper panels: orange (red) lines represent the swarm model with collection scheme I (II). The line types indicate the mean number of swarms per grid point ( $N_p/N_{\text{grid}}$ ); the total number density of physical particles is kept the same for all simulations by changing the number density of particles in each swarm and the number of swarms; see Runs 4A, 4C, 4D, 4E, 4F and 4G of Table B.2 for simulation details. Lower panels: similar to the upper panels, but for  $N_p/N_{\text{grid}}=4$  and different total numbers of swarms, as indicated by the line types; the corresponding  $N_{\text{grid}}$  is  $8^3$  (solid curve),  $16^3$  (dotted curve),  $32^3$  (dashed curve),  $48^3$  (dash-dotted curve) and  $64^3$  (dash-triple-dotted curve); see Runs 5A, 5B, 5C, and 5D of Table B.2 for simulation details.

This allows us to derive the following general formula

$$\frac{a_\zeta}{a_{\zeta/2}} = \left[ \frac{\prod_{\zeta'=\zeta/2+1}^{\zeta} (\mu + \zeta')}{\prod_{\zeta'=\zeta/2+1}^{\zeta} (\mu + \zeta')} \right]^{1/\zeta}. \quad (\text{F.2})$$

The expression on the right-hand side of this equation is a monotonic function of  $\mu$  and can easily be solved numerically. Once we know  $\mu$ , we compute  $\lambda$  via

$$\lambda = \frac{1}{a_\zeta} \left( \frac{\Gamma(\mu + \zeta + 1)}{\Gamma(\mu + 1)} \right)^{1/\zeta}. \quad (\text{F.3})$$

The resulting pairs of coefficients ( $\mu_\zeta, \lambda_\zeta$ ) are given in Table F.1 for Run 3C for different times and several values of  $\zeta$ . The moments used here are given in Table 2. The result for  $a_6/a_3$  is shown in Figure F.1, where we also compare with the result for  $a_2/a_1$ . The agreement between the two is surprisingly good.

## G The “bump” in the evolution of the mean particle radius

For the following discussion, it is convenient to introduce the unscaled moments

$$M_\zeta = \sum f(r) r^\zeta. \quad (\text{G.1})$$

so that  $a_\zeta = (M_\zeta/M_0)^{1/\zeta}$  and  $\bar{r} = a_1$ , as before. Let us now assume a situation with pure collection such that the total volume of water in the droplets is conserved. This implies that

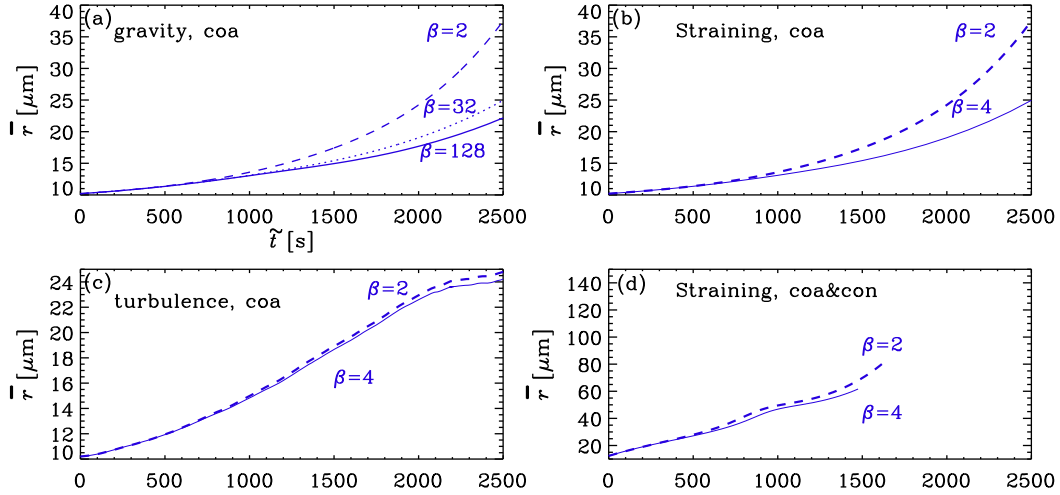


**Figure E.1.** MBR dependency for simulations with different flow pattern. Upper left panel: collection driven by gravity using  $k_{\max}=3457$  and  $\beta=128$  (solid),  $k_{\max}=865$  and  $\beta=32$  (dotted), as well as  $k_{\max}=55$  and  $\beta=2$ ; see Runs 3A and 3B of Table B.2 and 3C of Table 1 for simulation details. Upper right panel: collection driven by straining flow using  $k_{\max}=109$  and  $\beta=4$  (dashed line),  $k_{\max}=55$  and  $\beta=2$  (solid line); see Runs 8A and 8F of Table B.2 for simulation details. Low left panel: collection driven by turbulence using  $k_{\max}=109$  and  $\beta=4$  (dashed line),  $k_{\max}=55$  and  $\beta=2$  (solid line); see Runs 10E of Table B.2 and 10A of Table 1 for simulation details. Low right panel: collection driven by straining flow with condensation using  $k_{\max}=109$  and  $\beta=4$  (dashed line),  $k_{\max}=55$  and  $\beta=2$  (solid line); see Runs 8G of Table B.2 and 9D of Table 1 for simulation details.

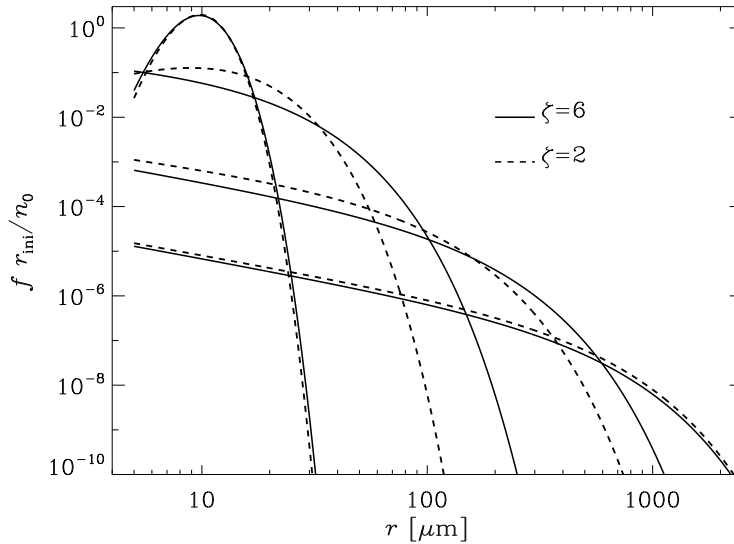


**Figure F.1.** Similar to Figure 5, but here we compare the Eulerian simulation with gamma distributions with coefficients obtained from  $a_2/a_1$  (solid line) and  $a_6/a_3$  (dashed line).

$M_3$  is constant, while  $M_0$  and  $M_1$  will always decrease with time. However, the relative rates at which  $M_0$  and  $M_1$  decrease can change. Indeed, a bump in  $\bar{r}$  is observed if  $M_1$  switches

**Table F.1.** Results for  $(\mu_\xi, \lambda_\xi)$  for different times.

$t$	2	4	6	12	24
0	(23.61, 2.412)	(22.50, 2.306)	(21.57, 2.218)	(18.74, 1.967)	(13.47, 1.547)
1	(2.16, 0.242)	(0.20, 0.108)	(-0.33, 0.079)	(0.03, 0.093)	(3.25, 0.159)
2	(-0.69, 0.017)	(-0.91, 0.009)	(-0.88, 0.010)	(-0.49, 0.014)	(1.91, 0.023)
3	(-0.92, 0.003)	(-0.94, 0.002)	(-0.90, 0.003)	(-0.33, 0.005)	(4.39, 0.010)

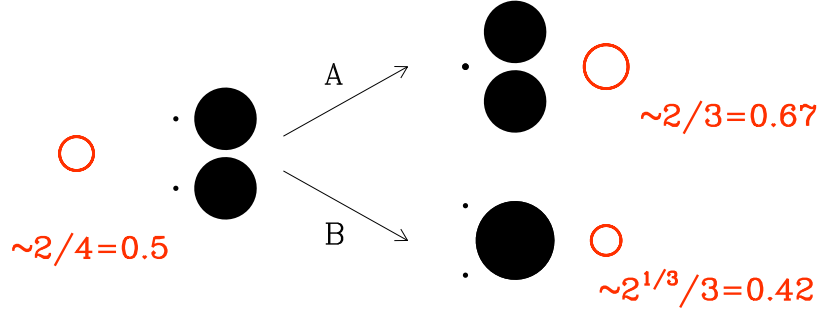


**Figure G.1.** Sketch illustrating the growth of  $\bar{r}$  when two small particles collide (A) and the decrease of  $\bar{r}$  when two large particles collide (B). Filled black symbols denote actual particle sizes and open red symbols and red text refer to  $\bar{r}$ .

from decreasing more slowly with time than  $M_0$  to decreasing faster than  $M_0$ . An example of such a situation will be presented in the following.

For a flow with two small and two large particles, with radii  $r_S$  and  $r_L$ , respectively, the size distribution is given by  $f(r) = 2\delta_{r,r_S} + 2\delta_{r,r_L}$ , where  $\delta_{ij}$  denotes the Kronecker delta ( $\delta_{ij} = 1$  for  $i = j$  and 0 otherwise). From equation G.1 it can then be found that the initial number of particles and sum of particle radii is given by  $M_0(0) = 4$  and  $M_1(0) = 2r_S + 2r_L$ , respectively. This yields a mean initial particle radius of  $\bar{r}(0) = M_1(0)/M_0(0)$ . In the following, we assume that  $r_S \ll r_L$ , so that  $\bar{r}(0) \approx 2r_L/4 = 0.5r_L$ .

When two particles of radius  $r_0$  collide, their combined mass is unchanged, so  $2r_0^3 = r^3$ , i.e., the target radius becomes  $r = 2^{1/3}r_0$  [Lamb and Verlinde, 2011]. Let us now consider two different collection scenarios; cf. Figure G.1. In scenario A, two smaller particles collide such that  $M_0(A) = 3$  and  $M_1(A) = 2^{1/3}r_S + 2r_L$ , while in scenario B two larger particles collide such that  $M_0(B) = 3$  and  $M_1(B) = 2r_S + 2^{1/3}r_L$ . Since  $r_L \gg r_S$ , we find for  $\bar{r}$  in both scenarios

$$\bar{r}(A) = (2^{1/3}r_S + 2r_L)/3 \approx 2r_L/3 \approx 0.67r_L > \bar{r}(0), \quad (\text{G.2})$$

$$\bar{r}(B) = (2r_S + 2^{1/3}r_L)/3 \approx 2^{1/3}r_L/3 \approx 0.42r_L < \bar{r}(0). \quad (\text{G.3})$$

This means that for scenario A the mean particle radius is increasing, while for scenario B it is decreasing. After the time when the bump appears in the time evolution of the mean particle radius (see Figure 8), it is primarily the heavier particles that continue collecting.

## H Self-collection in the Eulerian model

We recall that there are no self-collections in the usual Eulerian scheme. The potential importance of this can be assessed by comparing with calculations in which self-collection

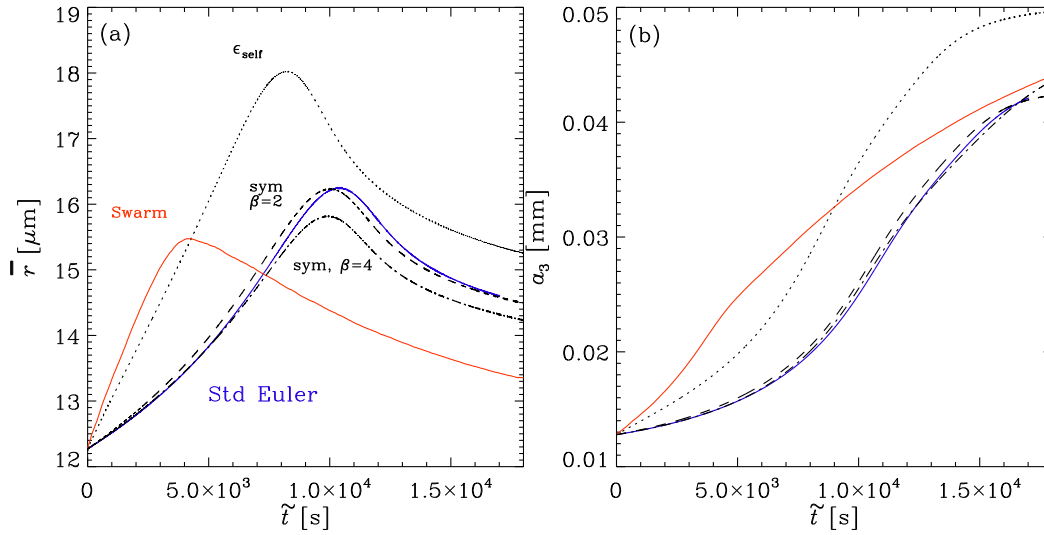


**Figure H.1.** Similar to the Eulerian model in Figure 6, but with self-collection invoked. Comparison of purely collectional growth for Eulerian models with average self-collection ( $\epsilon_{\text{self}}=0.01$ ) and symmetric self-collection (dashed for  $\beta=2$  with  $k_{\text{max}}=53$  and dash-dotted for  $\beta=4$  with  $k_{\text{max}}=109$ ), as well as the swarm model in a straining flow. Here,  $u_{\text{rms}} = 0.7 \text{ m s}^{-1}$ ,  $\tau_{\text{cor}} = 1.4 \text{ s}$ , while  $\tau_{\text{coll}} \approx 100 \text{ s}$ . The side length of the 2-D squared domain is  $L=2\pi \text{ m}$ . The parameters of the Eulerian model are  $n_0=10^{10} \text{ m}^{-3}$ ,  $r_1 = 4 \mu\text{m}$ , and  $r_{\text{ini}} = 12 \mu\text{m}$ . Those for the swarm model are  $N_p = 50000$  and NGP mapping is employed. See Runs 8A, 8B, 8C, 8D, and 8E of Table 1 for simulation details.

is included either via methods (i) or (ii); see the end of section 2.4 for their definitions. It turns out that by taking self-collection into account, method (i) causes only a weak speed-up in the increase of  $\bar{r}$ ; see Figure H.1. With method (ii), on the other hand, we find a strong enhancement of the growth. However, although method (ii) consists of an artificial manipulation of the diagonal terms of  $K_{ij}$ , it does not prove that self-collection is important, because similar manipulations of the off-diagonal terms of  $K_{ij}$  can have the same effect. In any case, this unphysical approach does not provide a proper solution to the convergence problem. We mention in passing that for this straining flow the effect of the  $\mathcal{M}_k$  term in equations (35) and (37) has no effect within plot accuracy.

## References

- Andrejczuk, M., J. M. Reisner, B. Henson, M. K. Dubey, and C. A. Jeffery (2008), The potential impacts of pollution on a nondrizzling stratus deck: Does aerosol number matter more than type?, *Journal of Geophysical Research: Atmospheres*, *113*(D19), n/a–n/a, doi:10.1029/2007JD009445, d19204.
- Andrejczuk, M., W. W. Grabowski, J. Reisner, and A. Gadian (2010), Cloud-aerosol interactions for boundary layer stratocumulus in the Lagrangian cloud model, *Journal of Geophysical Research: Atmospheres*, *115*(D22), n/a–n/a, doi:10.1029/2010JD014248, d22214.
- Arabas, S., and S. Ichiro Shima (2013), Large-eddy simulations of trade wind cumuli using particle-based microphysics with Monte Carlo coalescence, *Journal of the Atmospheric Sciences*, *70*(9), 2768–2777, doi:10.1175/JAS-D-12-0295.1.
- Babkovskaia, N., M. Boy, S. Smolander, S. Romakkaniemi, U. Rannik, and M. Kulmala (2015), A study of aerosol activation at the cloud edge with high resolution numerical simulations, *Atmosph. Res.*, *153*, 49–58, doi:10.1016/j.atmosres.2014.07.017.

- Bec, J., S. S. Ray, E. W. Saw, and H. Homann (2016), Abrupt growth of large aggregates by correlated coalescences in turbulent flow, *Phys. Rev. E*, *93*, 031,102, doi:10.1103/PhysRevE.93.031102.
- Berry, E. X., and R. L. Reinhardt (1974), An analysis of cloud drop growth by collection: Part i. double distributions, *Journal of the Atmospheric Sciences*, *31*(7), 1814–1824, doi:10.1175/1520-0469(1974)031<1814:AAOCDG>2.0.CO;2.
- de Lozar, A., and L. Muessle (2016), Long-resident droplets at the stratocumulus top, *Atmospheric Chemistry and Physics*, *16*(10), 6563–6576, doi:10.5194/acp-16-6563-2016.
- Drażkowska, J., F. Windmark, and C. P. Dullemond (2014), Modeling dust growth in protoplanetary disks: The breakthrough case, *Astron. & Astrophys.*, *567*, A38, doi:10.1051/0004-6361/201423708.
- Eibeck, A., and W. Wagner (2001), Stochastic particle approximations for Smoluchowski’s collection equation, *The Annals of Applied Probability*, *11*(4), 1137–1165.
- Elperin, T., N. Kleeorin, B. Krasovitov, M. Kulmala, M. Liberman, I. Rogachevskii, and S. Zilitinkevich (2015), Acceleration of raindrop formation due to the tangling-clustering instability in a turbulent stratified atmosphere, *Phys. Rev. E*, *92*(1), 013012, doi:10.1103/PhysRevE.92.013012.
- Falkovich, G., A. Fouxon, and M. G. Stepanov (2002), Acceleration of rain initiation by cloud turbulence, *Nature*, *419*, 151–154, doi:10.1038/nature00983.
- Geoffroy, O., J.-L. Brenguier, and F. Burnet (2010), Parametric representation of the cloud droplet spectra for les warm bulk microphysical schemes, *Atmospheric Chemistry and Physics*, *10*(10), 4835–4848, doi:10.5194/acp-10-4835-2010.
- Grabowski, W. W., and L.-P. Wang (2013), Growth of cloud droplets in a turbulent environment, *Ann. Rev. Fluid Mech.*, *45*(1), 293–324, doi:10.1146/annurev-fluid-011212-140750.
- Haugen, N. E. L., A. Brandenburg, and W. Dobler (2004), Simulations of nonhelical hydro-magnetic turbulence, *Phys. Rev. E*, *70*(1), 016308, doi:10.1103/PhysRevE.70.016308.
- Johansen, A. (2004), *Ice condensation, dust coagulation and vortex activity in protoplanetary discs*, Master’s thesis, Univ. Copenhagen.
- Johansen, A., A. C. Andersen, and A. Brandenburg (2004), Simulations of dust-trapping vortices in protoplanetary discs, *Astron. & Astrophys.*, *417*, 361–374, doi:10.1051/0004-6361:20034417.
- Johansen, A., J. S. Oishi, M.-M. Mac Low, H. Klahr, T. Henning, and A. Youdin (2007), Rapid planetesimal formation in turbulent circumstellar disks, *Nature*, *448*, 1022–1025, doi:10.1038/nature06086.
- Johansen, A., A. N. Youdin, and Y. Lithwick (2012), Adding particle collisions to the formation of asteroids and Kuiper belt objects via streaming instabilities, *Astron. & Astrophys.*, *537*, A125, doi:10.1051/0004-6361/201117701.
- Khain, A., M. Pinsky, T. Elperin, N. Kleeorin, I. Rogachevskii, and A. Kostinski (2007), Critical comments to results of investigations of drop collisions in turbulent clouds, *Atmospheric Research*, *86*(1), 1 – 20, doi:http://dx.doi.org/10.1016/j.atmosres.2007.05.003.
- Khain, A. P., K. D. Beheng, A. Heymsfield, A. Korolev, S. O. Krichak, Z. Levin, M. Pinsky, V. Phillips, T. Prabhakaran, A. Teller, S. C. van den Heever, and J.-I. Yano (2015), Representation of microphysical processes in cloud-resolving models: Spectral (bin) microphysics versus bulk parameterization, *Reviews of Geophysics*, *53*(2), 247–322, doi:10.1002/2014RG000468, 2014RG000468.
- Kumar, B., J. Schumacher, and R. A. Shaw (2014), Lagrangian mixing dynamics at the cloudy-clear air interface, *J. Atmosph. Sci.*, *71*(7), 2564–2580, doi:10.1175/JAS-D-13-0294.1.
- Lamb, D., and J. Verlinde (2011), *Physics and Chemistry of Clouds*, Cambridge, England, Cambridge Univ. Press.
- Lanotte, A. S., A. Seminara, and F. Toschi (2009), Cloud droplet growth by condensation in homogeneous isotropic turbulence, *Journal of the Atmospheric Sciences*, *66*(6), 1685–1697, doi:10.1175/2008JAS2864.1.
- Naumann, A. K., and A. Seifert (2015), A Lagrangian drop model to study warm rain microphysical processes in shallow cumulus, *Journal of Advances in Modeling Earth Systems*,

- 7(3), 1136–1154, doi:10.1002/2015MS000456.
- Naumann, A. K., and A. Seifert (2016a), Recirculation and growth of raindrops in simulated shallow cumulus, *Journal of Advances in Modeling Earth Systems*, pp. n/a–n/a, doi:10.1002/2016MS000631.
- Naumann, A. K., and A. Seifert (2016b), Evolution of the shape of the raindrop size distribution in simulated shallow cumulus, *Journal of the Atmospheric Sciences*, 73(6), 2279–2297, doi:10.1175/JAS-D-15-0263.1.
- Ogura, Y., and T. Takahashi (1973), The Development of Warm Rain in a Cumulus Model., *J. Atmosph. Sci.*, 30, 262–277, doi:10.1175/1520-0469(1973)030<0262:TADOWRI>2.0.CO;2.
- Ohtsuki, K., Y. Nakagawa, and K. Nakazawa (1990), Artificial acceleration in accumulation due to coarse mass-coordinate divisions in numerical simulation, *Icarus*, 83(1), 205 – 215, doi:http://dx.doi.org/10.1016/0019-1035(90)90015-2.
- Paoli, R., and K. Shariff (2009), Turbulent condensation of droplets: Direct simulation and a stochastic model, *Journal of the Atmospheric Sciences*, 66(3), 723–740, doi:10.1175/2008JAS2734.1.
- Patterson, R. I., W. Wagner, and M. Kraft (2011), Stochastic weighted particle methods for population balance equations, *Journal of Computational Physics*, 230(19), 7456 – 7472, doi:http://dx.doi.org/10.1016/j.jcp.2011.06.011.
- Pinsky, M. B., and A. P. Khain (1997), Turbulence effects on the collision kernel. I: Formation of velocity deviations of drops falling within a turbulent three-dimensional flow, *Quart. J. Roy. Met. Soc.*, 123, 1517–1542, doi:10.1002/qj.49712354204.
- Pruppacher, H. R., and J. D. Klett (2012), *Microphysics of Clouds and Precipitation: Reprinted 1980*, Springer Science & Business Media.
- Riechermann, T., Y. Noh, and S. Raasch (2012), A new method for large-eddy simulations of clouds with Lagrangian droplets including the effects of turbulent collision, *New Journal of Physics*, 14(6), 065,008.
- Saffman, P. G., and J. S. Turner (1956), On the collision of drops in turbulent clouds, *J. Fluid Mech.*, 1, 16–30, doi:10.1017/S0022112056000020.
- Sardina, G., F. Picano, L. Brandt, and R. Caballero (2015), Continuous Growth of Droplet Size Variance due to Condensation in Turbulent Clouds, *Phys. Rev. Lett.*, 115(18), 184501, doi:10.1103/PhysRevLett.115.184501.
- Seifert, A., and K. D. Beheng (2001), A double-moment parameterization for simulating autoconversion, accretion and selfcollection, *Atmospheric Research*, 5960, 265 – 281, doi:http://dx.doi.org/10.1016/S0169-8095(01)00126-0, 13th International Conference on Clouds and Precipitation.
- Seinfeld, J. H. (1998), *Atmospheric chemistry and physics of air pollution*, Cambridge, England, Cambridge Univ. Press.
- Seinfeld, J. H., and S. N. Pandis (2006), *Atmospheric chemistry and physics: from air pollution to climate change*, John Wiley & Sons, New Jersey.
- Shaw, R. A. (2003), Particle-Turbulence Interactions in Atmospheric Clouds, *Ann. Rev. Fluid Mech.*, 35, 183–227, doi:10.1146/annurev.fluid.35.101101.161125.
- Shima, S., K. Kusano, A. Kawano, T. Sugiyama, and S. Kawahara (2009), The super-droplet method for the numerical simulation of clouds and precipitation: a particle-based and probabilistic microphysics model coupled with a non-hydrostatic model, *Quart. J. Roy. Met. Soc.*, 135, 1307–1320, doi:10.1002/qj.441.
- Sullivan, N. P., S. Mahalingam, and R. M. Kerr (1994), Deterministic forcing of homogeneous, isotropic turbulence, *Phys. Fluids*, 6, 1612–1614, doi:10.1063/1.868274.
- Suttner, G., and H. W. Yorke (2001), Early Dust Evolution in Protostellar Accretion Disks, *Astrophys. J.*, 551, 461–477, doi:10.1086/320061.
- Svensson, G., and J. H. Seinfeld (2002), A numerical model of the cloud-topped marine boundary layer with explicit treatment of supersaturation-number concentration correlations, *Quart. J. Roy. Met. Soc.*, 128, 535–558, doi:10.1256/003590002321042081.
- Xue, Y., L.-P. Wang, and W. W. Grabowski (2008), Growth of cloud droplets by turbulent collision-coalescence, *Journal of the Atmospheric Sciences*, 65(2), 331–356, doi:10.1175/

2007JAS2406.1.

Zsom, A., and Dullemond, C. P. (2008), A representative particle approach to coagulation and fragmentation of dust aggregates and fluid droplets, *Astron. & Astrophys.*, 489(2), 931–941, doi:10.1051/0004-6361:200809921.